

NASA Contractor Report 189095

IN-24
84439
P-67

Inelastic Deformation of Metal Matrix Composites

Part I—Plasticity and Damage Mechanisms

B.S. Majumdar and G.M. Newaz
Battelle Memorial Institute
Columbus, Ohio

March 1992

Prepared for
Lewis Research Center
Under Contract NAS3-26053



(NASA-CR-189095) INELASTIC DEFORMATION OF
METAL MATRIX COMPOSITES. PART 1: PLASTICITY
AND DAMAGE MECHANISMS Final Report
(Battelle Memorial Inst.) 67 p

CSCL 11D

N92-22284

Unclass

G3/24 0084439

1

INELASTIC DEFORMATION OF METAL MATRIX COMPOSITES: PLASTICITY AND DAMAGE MECHANISMS

B. S. Majumdar and G. M. Newaz

Battelle Memorial Institute

Columbus, Ohio 43201

ABSTRACT

The deformation mechanisms of a Ti 15-3/SCS6 (SiC fiber) metal matrix composite (MMC) were investigated using a combination of mechanical measurements and microstructural analysis. The objectives were to evaluate the contributions of plasticity and damage to the overall inelastic response, and to confirm the mechanisms by rigorous microstructural evaluations. The results of room temperature experiments performed on 0-degree and 90-degree systems primarily are reported in this report. Results of experiments performed on other laminate systems and at high temperatures will be provided in a forthcoming report.

Inelastic deformation of the 0-degree MMC (fibers parallel to loading direction) was dominated by plasticity of the matrix. Grain boundaries and reaction-zone cracks were found to be important sites for dislocation and slip-band nucleation. In contrast to the 0-degree MMC, inelastic deformation of the 90-degree composite (fibers perpendicular to the loading direction) occurred by both damage and plasticity. This layup system had a characteristic three-stage deformation behavior: Stages I, II, and III. Inelastic deformation in Stage II was dominated by damage, in the form of fiber-matrix debonding and reaction-zone cracks. However, micro-yielding of the matrix also occurred in Stage II. In Stage III, plasticity was largely concentrated in intense shear bands between fibers. These ultimately led to shear crack initiation and failure. The predictions of a continuum elastic-plastic model were compared with the experimental data. The model was adequate for predicting the 0-degree response; however, it was inadequate for predicting the 90-degree response, largely because it neglected damage. The importance of validating constitutive models using a combination of mechanical measurements and microstructural analysis is pointed out. The deformation mechanisms, and the likely sequence of events associated with the inelastic deformation of MMCs, are indicated in this paper.

1. INTRODUCTION

Metal matrix composites (MMCs) have been the subject of intensive research in recent years. This stems from their excellent stiffness, strength, and wear properties, particularly at elevated temperatures.

In designing with MMCs, it is important to understand and model their constitutive response and failure conditions. Micro-mechanical and finite element method (FEM) techniques have been used to model the stiffness [Hashin and Rosen 1964, Hashin 1979, Adams and Doner 1967], strength [Kelly and Tyson 1965, Kelly 1972], and inelastic stress-strain behavior [Hill 1964, Adams 1970, Aboudi 1984, Chamis and Hopkins 1988, Robinson, Duffy and Ellis 1987, Dvorak and Bahei-El-Din 1982, Pindera and Lin 1989, Walker, Jordan and Freed 1989, Sun 1989, Nimmer et al. 1990] of MMCs. Except for Chamis et al.'s [Chamis and Hopkins 1988] and Nimmer et al.'s [Nimmer et al. 1990] models, which can account for limited damage, most of the inelastic models assume *a priori* that the inelastic deformation response of MMCs is due to plasticity/viscoplasticity of the matrix. However, composites are prone to damage in the form of debonding, delamination, void formation and cracking. Such damage also can give rise to non-linear deformation, requiring that the constitutive response be modeled differently than plasticity.

Against this background, it is interesting to note that comparatively little has been done in subjecting the models to rigorous validation testing, to establish whether plasticity or damage is the dominant mode of deformation, and whether any model is sufficient to predict the inelastic deformation of a MMC. Some recent experimental work on a Ti 15-3/SCS6 composite has been reported by Johnson et al. [1988] and Lerch and Saltsman [1991]. However, plasticity and damage issues were not adequately addressed, although both the papers attempted to correlate model predictions with experimental stress-strain curves. As will be indicated in this paper, our own study shows that agreement between a model and a MMC's uniaxial stress versus longitudinal strain response is insufficient to establish whether a model is adequate. In fact, we have found that although a model may appear to be adequate for predicting stress-versus-longitudinal* strain data for a MMC, it

* Throughout this paper, longitudinal strain implies strain along the tensile axis of uniaxially loaded specimens, independent of the fiber orientation. The off-axis strains are those perpendicular to the tensile axis.

can be inadequate for predicting off-axis strains.

The complex structure of MMCs make it imperative that any model realistically take into account the important deformation mechanisms. Otherwise component design can be non-conservative. A particularly attractive feature of MMCs is that they are tailor-made materials, and their structure and processing conditions can be varied over a wide range of conditions to suit application needs. It is desirable to perform preliminary stress-strain calculations [Morel, Saravanos and Chamis 1990] to optimize a processing route for required material properties, provided that the material deformation mechanisms are properly addressed. Thus, from both design and MMC fabrication viewpoints, there is a critical need to understand how MMCs deform. This need formed the rationale for the work described here.

In this investigation, monotonic tension tests were performed on a model MMC material: a Ti-15V-3Cr-3Al-3Sn (Ti 15-3) weight percent alloy, reinforced with SiC (SCS6) fibers. Attention was focussed on two laminate configurations: 0-degree system, where all the fibers are parallel to the loading direction, and the 90-degree system, where all the fibers are perpendicular to the loading direction. The primary objective was to understand the mechanisms of monotonic deformation of MMCs; in particular, the morphology and relative magnitudes of plasticity and damage.

2. EXPERIMENTAL APPROACH

The approach that was taken in this work was to confirm the deformation behavior by a combination of mechanical experiments and microstructural evaluation. We shall illustrate this by a simple example.

Consider a 0-degree composite that is loaded uniaxially in the fiber direction, and let it possess a non-linear deformation response, shown schematically by the region BCD in Figure 1. Let it also be assumed that the deformation is either by plasticity of the matrix, or by damage. The latter could be in the form of cracking of fibers, or the matrix, or the fiber-matrix reaction zone, or debonding at the fiber-matrix interface. The question that is now posed is whether the inelastic deformation BCD is due to plasticity or damage.

One powerful test for distinguishing between plasticity and damage is to unload the specimen from the nonlinear zone, and to observe changes in the MMC stiffness. Thus, if plasticity was the deformation mode, then the unloading stiffness would be identical to the loading stiffness (unloading path CE). Conversely, if damage was dominant, then the unloading line would pass through the origin (unloading path CA). The practical problem with this discriminatory test is that it has not yet been established whether this technique will work for MMCs, which have a high loading of fibers and which have a high residual stress field to start with. For example, even if plasticity was dominant, inelastic deformation of the matrix during unloading could result in a nonlinear unloading line, thus making the interpretation of stiffness changes rather difficult. On the other hand, even if the dominant deformation mechanism was damage in the form of dispersed fiber cracks and cracking of the reaction zone, the slope change may not be resolvable experimentally; those involved in fracture mechanics research are quite familiar with experimental difficulties in trying to determine small crack extensions from compliance changes in specimens. Fiber crack-closure effects during unloading, coupled with large changes in the residual stresses in the fiber and matrix, could make the slope change sufficiently small rendering it unresolvable.

A second technique that can be used advantageously to distinguish between plasticity and damage, and which also relies on mechanical measurements, is based on evaluating the Poisson's contraction of the specimen. The Poisson's ratio of engineering alloys increase from approximately 0.3 in the elastic stage to approximately 0.5 in the plastic stage of deformation. Although a 0-degree composite would not show a similar increase when the matrix became plastic, it is expected that the Poisson's ratio would increase if plasticity was the dominant mode of deformation. Experimental and analytical verification of this concept for an elastic-plastic system was demonstrated by Hamilton et al. [1971] for a model concentric cylinder system, loaded along the axis of the cylinders. On the other hand, if damage occurred in the form of cracks perpendicular to the loading axis, the Poisson's ratio would decrease. The reason is the cracks would make the material more compliant in the loading direction, without at the same time having any effect on the stiffness parallel to the crack plane; the net result is an increase in the Poisson's ratio. Figure 2 shows schematically the types of anticipated behavior if inelastic deformation was due to plasticity and damage. Although this technique has not been utilized in the past, we believe it can be a powerful tool to distinguish between plasticity and damage of MMCs. The advantage over the compliance technique is that the Poisson's ratio can be continuously monitored,

and no intermediate unloadings are necessary.

In addition to the two techniques above, metallurgical evaluation can be used to distinguish between plasticity and damage. Thus, if plasticity was the inelastic deformation mechanism, then cracks would not be observed if the specimen was unloaded before fracture and metallurgically polished. Conversely, if damage occurred, then cracks and debonds would be observed in the tested specimen. However, this technique may not be a sufficient test by itself, because even if damage was the dominant deformation mechanism, residual stresses could close the cracks and make them undetectable. One could then wrongly interpret the absence of cracks as an indication that inelastic deformation was due to plasticity.

From a metallurgical standpoint, confirmation of plasticity can come from observation of dislocation structures by transmission electron microscopy (TEM). Thus, if the matrix of the deformed MMC shows a dislocation structure different from that of the undeformed material, then plasticity is confirmed. The difference in dislocation structure could either be in the form of dislocation pile-ups, cell structure, or dislocation debris in the deformed material, as well as differences of dislocation densities. In interpreting TEM micrographs it must be recognized that TEM samples are obtained from a minute region of the material. Thus, there is a need to evaluate different regions of the test specimen to confirm that the dislocation structures are representative of the untested and tested materials.

Some matrix alloys show slip bands when plastically deformed. Under such conditions, optical microscopy also can be used to confirm plasticity. However, the converse is not true, in that even if plasticity was dominant, slip bands may not be observed.

Another technique for distinguishing between plasticity and damage is through micromechanical/FEM modeling. The method is indirect, in that an assumed model, based either on plasticity or damage, is used to predict the stress-strain response of a MMC, and the mechanism of deformation is inferred from the model that provides best correlation with the material's actual mechanical response. However, this approach can provide erroneous results if used indiscriminately and without adequate validation. A more dependable approach is to actually observe the MMC deformation mechanisms, and to use the modeling approach only for further confirming the mechanisms involved.

Table 1 is a survey of the above techniques for evaluating the material deformation mechanisms. Although the list is by no means complete, Table 1 contains many of the important characteristics of plasticity and damage. The central point is that the deformation mechanism must be confirmed by a combination of techniques, rather than relying on one technique alone. When both plasticity and damage are operative, the reference Table 1 can be utilized for identifying and quantifying the relative magnitudes of each deformation mechanism.

The mechanisms of deformation are anticipated to be dependent on the ply-layup. However, the type of layup would not alter significantly the way plasticity and damage are manifested, the former being associated with slip bands and changed dislocation densities, and the latter being associated with cracks and debonding. The primary modification in Table 1 would have to be with respect to the Poisson's ratios. Thus, in the case of the 90-degree MMC, the stiff fibers would prevent matrix contraction, even when plasticity was the dominant deformation mechanism. Consequently, the Poisson's ratio in the fiber direction would decrease even under plasticity. Hence, the Poisson's ratio for the 90-degree system would have to be more carefully analyzed before arriving at a conclusion regarding plasticity or damage.

Most current fiber-reinforced MMCs are only 1 to 3 mm thick. Therefore, for the sake of simplicity, we shall henceforth refer to the in-plane strain, perpendicular to the loading and thickness directions, as the width strain; and the out-of-plane strain, perpendicular to both the loading and fiber directions, as the thickness strain. Please refer to Figure 3 for definitions of the strain components. For the 90-degree MMC, the width strain would be parallel to the fibers. Since the thickness strain of the 90-degree MMC is not constrained by stiff fibers, the thickness Poisson's ratio would increase with plasticity and decrease with damage.

In this program, the mechanisms of monotonic deformation of the 0-degree and 90-degree MMC were evaluated using the methods outlined above. Specimens were loaded uniaxially, and strains were measured in the length, width, and thickness directions of the MMCs. Unloading was performed at different stages of deformation for measuring changes in specimen stiffness, and also for microstructural evaluation. Experiments were performed both at room temperature and at elevated temperatures; however, the emphasis in this paper is on room temperature experiments. The results of the mechanical and

microstructural studies, comparisons with analytical models, and our current understanding regarding the mechanism of deformation, are provided here.

3. EXPERIMENTAL PROCEDURES

The material tested was an 8-ply unidirectional Ti 15-3/SCS-6 composite, approximately 1.99 mm thick, fabricated by Textron (serial number 890556), using a foil-fiber-foil consolidation technique; the fiber volume fraction is approximately 0.34. The SCS-6 (SiC) fiber diameter is approximately 140 μm , and it contains alternating outer layers of C and Si, which protect the fiber from cracking during handling. The Ti 15-3 (Ti-15V-3Cr-3Al-3Sn, all in weight percent) alloy is a metastable body centered cubic (bcc) beta Ti-alloy, the bcc phase being stabilized by V.

Uniaxial tensile test specimens were machined from the unidirectional panel using an electric-discharge machining (EDM) technique; specimen dimensions are shown in Figure 3. The specimens were mechanically polished after EDM cutting to remove any damage associated with the machining. Specimens were prepared with two different orientations: 0-degree and 90-degree. In addition, Ti 15-3 matrix specimens, which were fabricated using the same foil layup process as composite panels, were tested. All specimens were tested in the as-fabricated condition, involving a cooldown from the HIP-ing temperature of approximately 815 C; no heat-treatment was performed prior to the testing.

Specimens were gripped using friction grips, and loaded on a servohydraulic testing machine at a strain rate of approximately 0.002/sec. The longitudinal and width strains were measured using both strain gages and extensometers; the thickness strains were monitored using an extensometer calibrated over a full scale range of 25 μm . Induction heating was used for performing experiments at elevated temperatures.

Following mechanical testing, specimens were sectioned slowly using a diamond wafering blade; significant debonding and fiber cracking can occur during machining if adequate care is not taken during sectioning. Sections were made perpendicular to the specimen axis (transverse cross section), and the center of the specimen width, but parallel to the specimen axis (edge cross section). This latter cross-sectioning technique was performed to reveal the bulk behavior, rather than effects associated with edges of mechanical test

specimens. Specimens were metallographically polished, with the polished surfaces corresponding either to the face of the test specimen, or the edge and transverse cross sections. Faces were polished at the surface as well as up to the first set of fibers. Repeated polishing was performed on a few tested and untested samples to confirm that cracking, debonding, or slip bands were due to deformation alone, and not associated with the polishing procedure. Specimens were etched using Kroll's reagent, which was found to be effective in revealing slip bands. Metallographic specimens were examined optically and also using a scanning electron microscope (SEM).

In addition to metallographic techniques, specimens were examined using transmission electron microscopy (TEM). Thin strips were cut using a wafering blade, and circular discs were machined from them using diamond paste and a slurry drill. These were then polished using a combination of ion milling and jet electropolishing. The electrolyte was a solution of 4 percent sulfuric acid in methanol and maintained between -15 C and -20 C. The voltage used was approximately 30 V and the current density was approximately 60 mA/mm². TEM specimens were examined on a JEOL microscope operating at 200 kV.

4. RESULTS

4.1 Mechanical Test Results

4.1.1. 0-Degree Composite: Figure 4 shows the stress-strain curves for four 0-degree specimens, where the longitudinal strains correspond to those measured by the extensometer. Three of the specimens were tested at Battelle, and the fourth was tested by Lerch et al. [1991] at NASA Lewis Research Center*. Figure 4 illustrates excellent reproducibility of stress-strain curves for the 0-degree MMC, with nonlinear deformation starting at a strain of approximately 0.55 percent.

In Figure 4, specimen 0-9 was partially unloaded from a total strain of approximately 0.55 percent (point B), then reloaded to failure. Specimen 0-1 was completely unloaded from a higher value of total strain (point D, 0.8 percent). Calculation of the slopes of the loading

* Lerch et al. (1991) tested a Ti 15-3/SCS6 composite, which was aged at 700 C for 24 hours in vacuum.

and unloading lines indicated that the stiffness of the specimens were essentially constant, with an effective elastic modulus of 176.5 GPa. In addition, there were significant strain offsets at zero load when specimens were unloaded from the inelastic regime of deformation. Thus, these results appear to indicate that the primary inelastic deformation mode was plasticity.

Figure 5 is a plot of the width strain versus the longitudinal strain for three 0-degree specimens. Both the strain gage and the width extensometer provided identical data. The width and thickness strains were always negative (both for the 0-degree and 90-degree specimens); however, in all subsequent plots on transverse (width or thickness) strains in this paper, the negative of transverse strains have been plotted, for clarity of presentation. The arrow in Figure 5 indicates approximately the strain value where nonlinearity started in the stress-versus-longitudinal strain curves. Solid lines have been sketched in the figure for specimen 0-N11, to better illustrate that the width strain increased at a higher rate after the nonlinearity point than before the nonlinearity point. The main point to note is the increase in slope rather than decrease in slope, implying that plasticity probably was dominant in the inelastic regime of deformation.

Figure 6 is a plot of the thickness strain versus the longitudinal strain for two 0-degree specimens. Specimen 0-9 had undergone an intermediate unloading at a strain of approximately 0.5 percent, and the plot shows that the thickness strain was almost fully reversible in the elastic regime. The changes in slope for specimen 0-6 at longitudinal strains of 0.005 and 0.008 are probably not significant since they were not observed in other specimens. The more important point to consider is whether the strains indicate specific trends during the elastic and inelastic regimes of deformation. Figure 6 illustrates that the thickness Poisson's ratio was high and approximately constant throughout the entire loading history, with no significant decrease in the inelastic domain.

4.1.2. 90-Degree Composite: Figure 7 illustrates the stress-strain behavior for four 90-degree specimens. Once again, the figure illustrates excellent reproducibility of the stress-strain response.

The 90-degree specimens showed a characteristic **three-stage** stress-strain behavior : Stage I (region AB) of high slope, Stage II (region BC) of a reduced slope, and finally

Stage III (region CD) of almost zero slope, the latter having the characteristic of a perfectly plastic solid. In Stage I, the strain was fully recoverable on unloading, and the composite behaved essentially as a linear-elastic solid. The elastic modulus was obtained as approximately 111 GPa.

The data for the specimen (90-20) unloaded from a total strain of 0.5 percent, shows that the unloading slope was 43 percent less than the loading slope. This would imply that damage is likely dominant during Stage II of deformation for the 90-degree composite, at least up to point E. However, Figure 7 illustrates that there also was a small strain offset (approximately 0.05 percent) at zero load. This would suggest that plasticity also may be present during Stage II.

Specimen 90-16 in Figure 7 was unloaded from Stage III of the stress-strain curve. The unloading stiffness for this specimen was approximately 56 percent less than the original loading stiffness, compared with a 43 percent stiffness loss for specimen 90-20, which was unloaded from Stage II. Thus, in proceeding from point E to G, the unloading stiffness dropped by 13 percent. On the other hand, the zero load offset for specimen 90-16 was approximately 0.23 percent, which was almost 4.5 times that for specimen 90-20. Thus, these results indicate that deformation in Stage III is controlled by both plasticity and damage, with the former likely playing a more dominant role.

Figure 8 is a plot of the width strain versus the longitudinal strain for two 90-degree specimens. This plot is very similar to Figure 7, illustrating the three-stage segmental nature of the 90-degree MMC. The slopes of the curves correspond to the instantaneous Poisson's ratios in the width direction. Figure 8 indicates that there was a sudden drop in the width Poisson's ratio in going from Stage I to Stage II, and that it approached zero in Stage III. A decrease in the width Poisson's ratio for the 90-degree composite does not necessarily imply damage, in contrast to the case of 0-degree specimens (see Figure 2). However, as will be shown later, the decreases in Poisson's ratio were too large to be explained by a plasticity mechanism alone.

Figure 9 is a plot of the total thickness Poisson's ratio, defined as the total thickness strain divided by the total longitudinal strain, for two 90-degree specimens. The plots show a gradual increase in the ratio as the material was deformed into the inelastic regime of deformation (past 0.2 percent strain), in contrast to the case of the width strain. The

increase in the thickness Poisson's ratio in Stages II and III indicates that the matrix was undergoing plastic deformation, and that some plasticity was present even in Stage II. The latter behavior is consistent with the small strain offset that was observed in Figure 7, when a specimen was unloaded from Stage II.

4.1.3. Ti 15-3 Matrix: Figure 10 is a stress-strain plot for the Ti 15-3 matrix material, illustrating an almost elastic-fully plastic behavior for the matrix material; the specimen was not loaded to failure. The matrix modulus was approximately 90.3 GPa. The width and thickness strain data are not plotted here, but they showed the anticipated increases in the Poisson's ratios as the material was deformed from the elastic into the plastic regime of deformation. The elongation to failure of the matrix material was approximately 12 percent.

In summary, the mechanical measurements suggest that plasticity likely was dominant in the inelastic regime of deformation for the 0-degree composite. In contrast, the 90-degree composite exhibited characteristics of both damage and plasticity. The former likely was the dominant mechanism in Stage II, and the latter likely was the dominant mechanism in Stage III.

4.2. Microstructure

4.2.1. As-Received Material : Figures 11a and 11b are longitudinal and transverse sections of the as-received material. The regions indicated by A, B, and C correspond to the fiber, reaction zone, and matrix, respectively. Dark lines, such as shown by D, correspond to the outer carbon layer of the fiber. Observations at higher magnification indicate they (D) are not debonded regions. They appear dark partly because of surface relief; the matrix tends to polish faster than the fiber. In Figure 11, the feature that we would like to emphasize is that the material is free of cracks or any obvious debonding or damage; thus the polishing procedure does not appear to have introduced any defect in the microstructure.

Figures 12a and 12b are corresponding etched microstructures of the as-received material. There is no indication of slip bands in the as-received microstructure. The small needle-shaped particles are different intermetallic compounds and precipitated alpha phase; they did not play any role in so far as damage development or plasticity nucleation was concerned.

The arrow in Figure 12a shows a grain boundary (gb). In addition, there was a blocky type of phase (most likely titanium carbides, based on previous studies at Battelle [Majumdar and Newaz 1991]) along the ply-to-ply interfaces (indicated by arrow A in Figure 12b), i.e., in those zones where the Ti 15-3 foils had bonded during the hot isostatic pressing (HIP) operation at approximately 815 C. Such zones are regions for potential cracks under thermo-mechanical fatigue loading, as pointed out previously by Majumdar and Newaz [1991].

4.2.2. Deformed 0-Degree Composite: Figure 13 shows the etched microstructure of the Ti-alloy surface of a 0-degree specimen, unloaded from a total strain of approximately 0.9 percent. Slip bands, indicated by the abbreviation 'sb' in the figures, may be observed emanating from the grain boundaries. This confirms that plasticity was present, and that grain boundaries were strong sources for dislocation emission.

Figure 14 shows the microstructure of a 0-degree specimen that was polished down to the first set of fibers. This specimen also was unloaded from approximately 0.9 percent strain. The photo micrograph illustrates two important points: (i) there were no fiber cracks, at least up to a total strain of 0.9 percent, and, (ii) there was widespread matrix plasticity, as evidenced by the numerous slip bands (see arrows). Thus, these microstructural features indicate that inelastic deformation of the 0-degree MMC was primarily through plastic deformation of the matrix.

Figure 15a is an optical micrograph at the fiber-matrix interface of a 0-degree composite that was strained to 0.9 percent. The figure illustrates slip bands (sb) which appear to nucleate from reaction-zone cracks (arrow A). This implies that in addition to grain boundary dislocation sources, reaction-zone cracks are another important source for dislocation nucleation. Figure 15b is a SEM micrograph of another region, showing slip bands nucleating from the matrix/reaction-zone interface. The three major slip bands in this figure are associated with reaction-zone cracks; the cracks have been highlighted by ink because they were only faintly visible (see arrow). However, the smaller and faintly visible slip bands between the major slip bands are not associated with cracks, indicating that reaction-zone cracks are not essential for nucleating slip bands from the fiber-matrix interface. The nonassociation of slip bands with reaction-zone cracks may be because the bulk matrix stress at 0.9 percent strain was sufficiently high to cause widespread plasticity.

In order to ascertain whether reaction-zone cracks were active in the elastic and micro-yield regime (at strains in the range 0.3-0.5 percent), we followed the slip band nucleation process using a surface replication technique. Those results indicate [Majumdar, Newaz and Ellis 1991, Newaz and Majumdar 1991] that some reaction-zone cracks nucleate at strains as low as 0.3 percent, but they appear to remain essentially inactive up to a strain of approximately 0.45 percent. Optical and SEM observations failed to provide any evidence of localized plasticity in grains that later revealed extensive slip bands. Beyond 0.45 percent strain, the reaction-zone cracks are able to nucleate minute slip bands of lengths roughly equal to those of the reaction-zone cracks; the slip morphology is similar to what is observed during blunting of cracked ductile metals. Only at strains between 0.5 and 0.6 percent do longer slip bands become easily observable and start having the appearance shown in Figures 14 and 15. The entire sequence indicates that the matrix awaits the development of a sufficient average stress before slip bands are observable at reaction zone cracks*. Although detailed TEM examination of the reaction-zone/matrix interface is needed, we were able to resolve slip bands as small as 1 μm . Thus, lack of any observable slip band below 0.45 percent strain in any grain (particularly those that revealed extensive slip band activity at strains above 0.5 percent) is indicative that plasticity likely is negligible below 0.45 percent strain.

At higher strains (0.6 percent and above), many more reaction-zone cracks nucleate, and they are almost always associated with slip bands. Simultaneously, grain boundary dislocation sources become active, indicating gross plastic deformation of the matrix material. It is possible that gross matrix plasticity may aid the formation of reaction-zone cracks at these higher strains. We base this possibility on the nonuniform spacing of reaction-zone cracks in going from one grain to the next (see Figure 15a). If matrix plasticity had no effect, then the reaction-zone cracks would likely have formed an equally spaced array (similar to what is observed in ceramic matrix composites), independent of the particular grain surrounding the fiber. On the other hand, from an iso-strain compatibility consideration, nonuniform plastic deformation in different grains would cause nonuniform strain (and stress) distribution along the length of a fiber, and likely show different reaction-zone crack spacing along the fiber length.

It was also observed that as the slip bands grew in size, the reaction-zone cracks became

* Simple fracture mechanics calculations indicate that the stress intensity factor at such cracks range between 1 and 4 $\text{MPa}\sqrt{\text{m}}$, which are small numbers.

larger and better defined. This may simply be a result of strain compatibility. Alternately, the back stress of dislocations could also have aided the growth of such cracks. Our current observations are not sufficient to pinpoint the exact sequence of matrix plasticity and reaction-zone cracks during this stage of deformation. However, since gross matrix plasticity is confirmed during this stage, reaction-zone cracks may not be as important for strains above 0.6 percent as those occurring below 0.5 percent (microyield domain).

Another notable feature of Figure 15a is the path of the reaction-zone crack. The region marked by the arrow, B, shows how the crack has deviated from the original plane into the fiber direction. The transition generally occurred at one of the carbon-silicon interfaces of the outer layers of the SCS6 fibers. Had this deviation not occurred, crack initiation from the reaction zone could have led to fracture of the fiber, and possibly to failure of the composite. Crack paths such as B in Figure 15a were quite frequent; in fact, at a number of locations, the deviated cracks joined together to provide the impression of a debonded fiber. More importantly, the crack paths do indicate that if brittle reaction zones cannot be avoided, then a weak or a ductile interface should be available to prevent any reaction zone cracks from propagating into the fiber.

Final failure of the 0-degree composite was precipitated by fiber fracture, so that an appropriate failure criteria for the composite would be the strain corresponding to fiber fracture. However, fiber failure appeared to be influenced by failure of Mo ribbons, which were used to hold the fibers in place during fabrication of the MMC; the Mo ribbons were spaced approximately 5 mm apart. Figure 16a shows the longitudinal cross section around the fracture surface. The cracked tear-drop shaped regions (only one half of the tears are visible in this fracture half) correspond to the Mo ribbon. Figure 16b corresponds to the same sample, away from the fracture surface, but around another Mo ribbon. This micrograph once again shows significant cracking of the Mo ribbon. It appears that Mo-ribbon fracture occurs prior to fiber failure; evidence for this sequence is the fact that fiber damage was observed at intervals of approximately 5mm, coinciding with locations where the Mo ribbons were placed. Also, the fracture surface showed Mo ribbons spanning the length of many plies (as many as six out of eight), indicating the preferred failure location. Thus, Mo ribbons, with limited ductility, are sources of weakness, and probably warrant replacement by a more ductile material.

Figures 17 and 18 are TEM images of the untested material. Although the micrographs

indicate the presence of dislocations, their density was quite low and there was very little evidence of any dislocation pileup. Thus, whatever inelastic deformation that occurred during cool-down from the processing temperature likely was insufficient to cause widespread plasticity of the matrix.

Figures 19a and 19b are, respectively, bright-field and dark-field TEM images of a foil prepared from a 0-degree specimen that was loaded to a total strain of 0.9 percent; the micrographs were taken around a [011] zone axis. The TEM foils were sectioned perpendicular to the tensile axis, and foil perforations corresponded approximately to the central regions of the cross section of the test specimen. Therefore, the micrographs are representative of the matrix material between the fibers.

In Figure 19a/19b, the line running from the top-left to the top-right of the micrograph corresponds to a grain boundary. The figures show a large number of dislocations emanating from the grain boundary. Many of the dislocation arrays had an inverse pileup type of configuration; the dislocation spacings, however, did not conform to theoretical predictions, likely because of relaxation of stresses associated with polishing of the TEM specimen. The large arrays of dislocations confirm that widespread plasticity of the matrix occurs when the 0-degree composite is loaded into the inelastic regime of deformation. Additionally, Figures 19a and 19b illustrate that grain boundaries were an important source for dislocation emission. Burgers vector analysis indicated that the dislocations were of the type [111], in agreement with the preferred Burgers vector for a bcc material at room temperature. Referring back to Figures 13 and 14, it is clear that the slip bands were easily observable because of the propensity of the matrix material to form dislocation-pileup type of configurations.

Figure 20, a TEM micrograph from another region of the test specimen, shows a number of intersecting pileups. We could trace the source of one of these pileups (the one that runs at 1 o'clock position) to a grain boundary. However, the source for the other two pileups remains uncertain; they appeared to emanate from the fiber-matrix interface, which was at the right of the micrograph. Efforts are currently under way to determine more rigorously the nature of dislocation emission from the reaction zone boundary. The significant point here is that both TEM and optical microscopy establish the occurrence of large dislocation activities in the 0-degree specimen loaded into the inelastic regime of deformation. This evidence, along with the absence of fiber or matrix cracks, confirm metallurgically that the

primary inelastic deformation mode of the 0-degree MMC was plasticity of the matrix, at least up to a strain of 0.9 percent. The only mechanism by which damage may have contributed to the overall strain was through cracking of the reaction zone. However, the cracking was limited to a small surface layer, so that the contribution of damage to the overall deformation response was likely small compared to the contribution of plasticity.

We have performed preliminary TEM analyses of the microstructure to understand the source for the observed concentrated slip (dislocation pile-up type of configurations), rather than diffused slip, in the Ti 15-3 matrix of the composite specimens. Observations at high magnifications with appropriate reflections showed an extremely fine precipitate structure in the matrix material. Although a detailed analysis of the shape and size of the fine precipitates was outside the scope of this investigation, we believe, based on the work of Silcock [1958], McCabe and Sass [1971], Sass (1969) and Blackburn and Williams [1968], that the fine precipitate structure corresponds to the ω -phase in the metastable bcc Ti-15V-3Cr-3Sn-3Al microstructure. The ω -phase is a hexagonal close-packed (hcp) phase, of size between 10 and 30 Å, with lattice parameters $a_{\omega}=(\sqrt{2})a_{\beta}$, and $c_{\omega}=(\sqrt{3}/2)a_{\beta}$; the orientation relations are $(0001)_{\omega} \parallel (111)_{\beta}$, and $[2\bar{1}\bar{1}0]_{\omega} \parallel [1\bar{1}0]_{\beta}$. It has been shown by McCabe and Sass [1971] that the coherent ω -particles are arranged in cluster of rows along $\langle 111 \rangle_{\beta}$ directions, and that this particular arrangement was responsible for $\{111\}$ lines of intensity (streaking) in reciprocal space for as-quenched Ti-V alloys. For the current material, in the as-fabricated condition, one would expect to see streaks from the $\langle 111 \rangle$ rows of ω -phase, if that phase was indeed present. The orientation of the streaks in the selected area diffraction pattern (SADP) would be parallel to the line drawn from the origin (000) to the plane formed by the zone axis and the $\langle 0001 \rangle_{\omega}$ or $\langle 111 \rangle_{\beta}$ directions. Figures 21a through 21d show the SADP of the Ti 15-3 matrix in the composite material for four different zone axes: $[110]$, $[111]$, $[120]$ and $[331]$. A few of the bcc β -reflections are numbered in the figures. The figures show streaks (lines) associated with ω -reflections; the streaks pass through specific β -reflections because those d-spacings coincide for both ω and β reflections (e.g. $(1\bar{1}\bar{2})_{\beta}$ and $(30\bar{3}0)_{\omega}$, or $(1\bar{1}0)_{\beta}$ and $(\bar{1}210)_{\omega}$). Additionally, the orientations of the streaks in each of the figures are in

agreement with those for the ω -phase being oriented along $\langle 111 \rangle$ directions; e.g., for the $[110]$ zone axis, the streaks in the SADP lie parallel to the line drawn from the origin to the $(1\bar{1}\bar{2})$ plane and $(1\bar{1}2)$ plane, both of which are formed by the zone axis and the $\langle 111 \rangle$ directions. Figure 21c shows three faint spots associated with specific ω -reflections.

In summary, the diffraction patterns in Figure 21 confirm the presence of the fine ω -phase in the Ti 15-3 matrix of the composite. A consequence of the fine and coherent ω -phase structure is that they are easily shearable by dislocations. Thus, a slip step left by a preceding dislocation favors the next dislocation to pass through the same location, rather than finding an alternate nearby route. It appears that this microstructural characteristic was responsible for concentrated slip and dislocation pileup type of configurations in the matrix material, rather than diffused slip. It was this concentrated slip, caused by the fine ω -phase, that likely made slip bands easily observable.

4.2.3. Deformed 90-Degree Composite : Figures 22a and 22b correspond to the edge cross section (at mid-width) of a 90-degree specimen that was loaded into Stage III. Significant fiber-matrix debonding may be observed, both at the outer and inner carbon layers. Radial cracks in the brittle reaction zone also may be observed, such cracking being necessitated by the large deformations that are seen to occur around the fibers. Although some of the fibers in Figure 22a appear not to have debonded, observations at higher magnification indicated that indeed all fibers had debonded. The surface kink (location A) in Figure 22a is a real effect, although the location was rounded during metallographic polishing. Such kinks/steps provided the appearance of cracks on the specimen faces, but no cracks were observed. It appears most likely that the surface steps resulted from localized plasticity between the specimen faces and the debonded matrix around the fibers.

Figure 23 is a longitudinal section of the same composite. This micrograph shows that, in addition to debonding, there was cracking in the reaction zone and in the outer Si-rich layer of the fiber. Many of the reaction-zone cracks had a saw-tooth appearance, which suggest that debonding is also associated with a cracking process, involving radial and axial cracking at inner and outer carbon layers. The crack-growth mode of debonding is also energetically favorable, because once a crack nucleates the load required for further

propagation of the crack would decrease with crack length.

Figure 24 shows the etched microstructure of a 90-degree specimen that was loaded into Stage III. The micrograph shows two types of slip bands: i) slip bands that are arranged in a triangle (shown by regions A in the figure), and give the appearance of slip line fields emanating from the fiber, and, ii) intense shear bands (shown by region B in the figure), that zig-zag between alternate fibers in adjacent plies. Observation of samples that were loaded into different regions in Stage III indicated that the triangular type of slip bands (Type A) occurred earlier, followed later by intense shear bands. In fact, final failure occurred by shear along the intense shear bands.

It is also of interest to note in Figure 24 that fibers in adjacent plies were not arranged in the form of a square array. Rather, the fibers in adjacent plies were staggered, which would make it easier for intense shear bands to form. Observation of other samples confirmed that the staggered fiber arrangement, shown in Figures 24, was quite frequent. It is possible that the staggered fiber arrangement may be a result of the MMC processing technique, where HIP-ing of the foil-fiber-foil system occurs by plastic shearing of the foil, which would favor a staggered arrangement of fibers by the same intense shear mechanism, or possibly by some instability process. Detailed investigation of the fabrication process is necessary to ascertain the source for the frequent staggered arrangement.

Figure 25 is an optical micrograph of an etched 90-degree sample that was loaded to a total strain of approximately 0.5 percent, corresponding to the middle of Stage II deformation; the loading axis is vertical in the figure. Slip bands (indicated by 'sb') may be observed nucleating preferentially at the reaction-zone cracks (see arrows), similar to what was observed for the 0-degree composite. We have used a surface replication technique to follow the initiation of reaction-zone cracks and slip band nucleation from such cracks. Those results (Majumdar et al. [1991] and Newaz et al. [1991]) indicate that the reaction-zone cracks start forming at strains between 0.4 and 0.5 percent, which is well into the middle of Stage II deformation. Thus, those slip bands are unable to explain the large drop in slope observed in going from Stage I to Stage II in the stress-strain curves. Observation of the top and bottom of the fibers did not indicate any obvious debonding, and it was suspected that the debond may have closed as the specimen was unloaded from Stage II.

To further clarify the mechanism of deformation in Stage II, a surface replication technique was adopted. Surface replicas were obtained at different values of load. Figure 26 is a SEM image of a replica that was obtained at a strain of 0.5 percent, i.e., in Stage II. The regions indicated by arrows are not fiber cracks. Rather, they represent the replication tape that had penetrated from the surface and entered into the specimen in the debonded regions. The penetration was localized only at the top and bottom of the fiber, indicating that those were the regions where debonding occurred. The resulting nonuniform penetration of the replica, and the stresses that were set up in the replica during drying, likely were responsible for the cusped and blob-type appearance of the replica at debonded regions. The specific locations of the debonds are also consistent with the fact that such locations experience the maximum tensile radial stress during loading, which would tend to debond the matrix from the fiber. Further confirmation that debonding and closure were operative in Stage II was obtained by taking a replica after the specimen was unloaded. Figure 27 is a SEM micrograph of another replica from the same region as Figure 26, after the specimen was unloaded from 0.5 percent strain. The regions marked by arrows show that there was no penetration of the replica, indicating that the debond had closed on unloading. These observations are consistent with the unloading curves shown in Figure 7.

An added feature that we would like to point out regarding Figures 26 and 27 is the small slip band activity at the top and bottom of fibers (see arrow marked sb). These slip bands appear to precede debonding. Their specific locations are consistent with elastic calculations, which indicate that in the 90-degree composite, the maximum effective stress in the matrix occurs at the top and bottom of fibers, rather than at locations 90 degrees with respect to the loading axis. It was also observed that after the debonding stage, these slip bands became dormant. This characteristic is again consistent with simple calculations of a hole stressed in an elastic solid.

In summary, the metallurgical evaluations indicate that the primary inelastic deformation mechanism in Stage II is fiber-matrix debonding. A similar conclusion was reached by Johnson et.al [1988]. However, more significant here is the slip band activity in Stage II, nucleated by premature cracking of the reaction zone. Such plasticity likely was responsible for the small strain offset that was observed at zero load. Clearly, in order to prevent premature plasticity, there is a need to improve the fiber-matrix interface/interphase property. In Stage III, plasticity played a more dominant role, and debonds were prevented from closing when the specimen was unloaded. Damage also increased in Stage III, but it

was aided by plasticity; i.e., cracking or debonding were not the primary drivers of inelasticity in Stage III, unlike in Stage II. During the later stages of Stage III, intense shear bands formed between fibers in adjacent plies. These ultimately led to formation of shear cracks in the matrix at the reaction-zone cracks, and their propagation to failure by a shear mechanism.

5. ANALYSES

We attempted to analyze the stress-strain response of the composites based on the observed deformation mechanisms. The results of a finite element method (FEM) analysis, which accounted for both damage and plasticity, will be published separately [Brust et al. 1991]. In this section, we show, as an example, how the predictions of a continuum-based elastic-plastic model agreed with the experimental data. The emphasis here is to illustrate that both plasticity and damage must be accounted for in any comprehensive model, and that rigorous validation is necessary before any model is accepted as being representative of the material behavior.

The model that we selected was the analytical model of Dvorak and Bahei-el-Din [1982], for which a computer code named AGLPLY is available. It is based on a vanishing fiber diameter model, and can be used effectively to predict lamina and laminate properties from the elastic-plastic response of the matrix and fiber materials. The primary drawback of the model is that it cannot account for damage. However, this drawback was useful in estimating how model predictions would be off from measured data, if damage did occur in the composite (primarily the 90-degree composite).

Figure 28 shows comparisons of the model predictions with experimental data for the 0-degree composite. The model predictions are good up to a strain of approximately 0.9 percent. Beyond that strain, the differences between the model predictions and the experimental results are significant. The reasons for those differences are not yet clear. They may be related to premature cracking of Mo ribbons, as well as reaction-zone cracks, which were not accounted for in the analyses. We would like to note, however, that the fiber stresses become greater than 2800 MPa for composite strains larger than 0.9 percent. Such stresses are close to the failure strength of fibers (approximately 3100 MPa), so that composite strains above 0.9 percent may not be of much practical significance.

The elastic-plastic model was good in predicting the measured yield strain of approximately 0.5 percent for the composite. This strain is less than the yield strain of approximately 0.8 percent for the matrix. The reason for this difference is the residual tensile stress in the matrix on cooling from the processing temperature. A simple micro-mechanical thermal residual-stress analysis, assuming that α and E remain constant with temperature, shows that the average mechanical strain in the matrix from cool-down is approximately

$$\epsilon_m = \delta\alpha \cdot \delta T / \{ (E_m V_m / E_f V_f) + 1 \} \quad (1)$$

where $\delta\alpha = \alpha_m - \alpha_f$ (greater than zero), $\delta T = T_F - T_o$, V_m and V_f are the volume fractions of the matrix and fiber, respectively, T_F is the fabrication temperature (815 C), and T_o is the test temperature (25 C). The subscripts m and f correspond to the matrix and fibers, respectively. A one-dimensional model, with no influence of transverse constraint stresses is assumed. Using $E_m = 90$ GPa, $E_f = 400$ GPa, $\alpha_m = 9 \times 10^{-6}/C$, and $\alpha_f = 4.5 \times 10^{-6}/C$, equation (1) yields a matrix mechanical strain of approximately 0.24 percent at room temperature. If this residual mechanical strain is added to the observed yield strain of 0.5 percent for the composite, we obtain a matrix strain of 0.74 percent at yielding of the composite. This value is close to the yield strain of approximately 0.8 percent for the matrix material. Thus, this simple residual stress analysis is able to provide a fairly good estimate of the average thermal residual axial stress, and more importantly provides a physical explanation as to why the macroscopic yield strain of the composite was in the range 0.5-0.6 percent rather than 0.8 percent.

More accurate 3-D analysis {Newaz, Majumdar and Brust (1991) and Brust et al.(1991)} reveal that in an extremely small zone surrounding the fiber, the effective residual stress is only slightly less (up to 100 MPa less) than the yield stress of the matrix. Thus, this region would be the first to yield on application of load. However, this locally highly stressed region had negligible effect on the yield stress of the composite; i.e., the yield strength was dominated by bulk plasticity of the matrix. Additionally, we observed that slip bands did not nucleate at strains below 0.45 percent, at which strain the highly stressed zones should be well into the plastic regime of deformation. Although additional TEM work is needed to confirm any lack of plasticity below 0.45 percent strain, our experimental observations

appear to indicate that the reaction-zone/matrix interface may possibly hinder dislocation nucleation. Also, the constraint of the surrounding fiber and matrix may have prevented dislocations nucleated in the highly stressed zone from penetrating into the surrounding matrix.

Figure 29 shows comparisons of the model predictions with the experimental data for the 90-degree composite. The figure illustrates that the model is excellent for predicting the longitudinal stress-strain response, at least up to a strain of 0.6 percent. This good correlation of the AGLPLY analysis is, however, surprising, since the microstructure of the composite showed clear evidence of fiber-matrix debonding in Stage II and Stage III of deformation.

Figure 30 is a plot of the instantaneous width Poisson's ratios (instantaneous slope of the width-strain-versus-longitudinal-strain plot) versus the longitudinal strain for the 90-degree composite. The experimental data, represented by dots, indicate that the initial Poisson's ratio was approximately 0.18. At longitudinal strains around 0.2 percent, the ratio dropped sharply, coincident with the start of Stage II deformation. The Poisson's ratio in Stage II was approximately 0.07. At larger strains, in Stage III, the ratio dropped even further and approached a value of zero. Figure 30 also shows predictions from the AGLPLY analysis and the FEM analysis of Brust et al.[1991]; the latter accounted for fiber-matrix debonding damage. Although the AGLPLY model appears adequate for predicting the initial Poisson's ratio, it is inadequate for predicting the Poisson's ratio in Stage II and Stage III.

The results of the AGLPLY analysis in Figures 29 and 30 illustrate the pitfalls of validating models using only the results of stress versus longitudinal strain measurements. If only Figure 29 was considered, then one might conclude that the model was satisfactory, and it could be used in design for calculating stresses and strains in critical locations (such as at the fiber-matrix interface). On the other hand, Figure 30 clearly points out that such a conclusion is faulty; in fact, the results would be highly nonconservative, since the model would predict lower stresses at the fiber-matrix interface, a region where final failure often initiates. Additionally, if one were to interpret deformation mechanisms based on the performance of theoretical models, then a totally wrong picture would emerge.

6. DISCUSSION

There were three primary objectives of the work described in this paper:

- (i) To understand the mechanisms of deformation of a MMC using key experiments and exhaustive microstructural examination.
- (ii) To evaluate the contributions of plasticity and damage to the overall deformation behavior. A literature survey had indicated that there was very little experimental evidence regarding which mechanism dominated, although a number of models assumed *a priori* one or the other.
- (iii) To evaluate existing and new models based on measured longitudinal and off-axis strains, and observed deformation mechanisms.

A Ti 15-3/SCS6 composite was chosen as a model material because it is a well developed system, and is anticipated to provide important insights into the deformation mechanisms of other Ti-alloy and Ti-aluminide based MMCs. Experiments were performed on the 0-degree and 90-degree systems, and the matrix material. Only monotonic tests were considered, to keep experimentation simple and relatively easy to analyze, and to avoid complications from reversed deformation, oxidation, and time-dependent effects.

The results presented here suggest that a detailed approach is able to provide a coherent picture of the deformation mechanisms. Thus, we have been able to establish that the inelastic deformation of the 0-degree MMC is dominated by plasticity of the matrix material. On the other hand, the 90-degree composite has a three-stage deformation response, with both damage and plasticity playing important roles.

The experimental results suggest that both the unloading compliance and Poisson's ratio techniques can be useful indicators of damage and plasticity of MMCs. However, it should be recognized that matrix cracks were few under monotonic loads, so that it is not certain whether mechanical measurements will be adequate to provide information on matrix cracking under, say, fatigue loading. In the absence of such data, we believe that detailed microstructural evaluation is imperative to confirm the occurrence of different inelastic deformation processes.

The dislocations (in TEM micrographs) and slip band features that were observed illustrate

the plasticity mechanisms in the Ti 15-3/SCS6 composite. To our knowledge, there is very little work in the literature which show clearly the plastic deformation morphology in fiber-reinforced MMCs. In addition to grain boundary sites, reaction-zone cracks also were found to be strong sources for dislocation nucleation. Consequently, it is important to focus attention on optimizing the fiber-matrix interface, to retard the formation of reaction-zone cracks. This factor becomes particularly important for intermetallic based composites, where the matrix may possess extremely low ductility, so that the reaction-zone cracks would precipitate brittle failure rather than slip bands. In this paper, we have not addressed the mechanics and morphology of dislocation nucleation from the matrix/reaction-zone interface. However, the experimental observations warrant a deeper understanding of dislocation nucleation from interfaces.

The modeling studies show that it is important to rigorously validate models using a combination of longitudinal strain and off-axis strain measurements. Thus, whereas the AGLPLY analysis was able to predict the stress-versus-longitudinal strain response of the 90-degree MMC, it was inadequate for predicting off-axis strains. This was because the analysis neglected damage, which was observed in the experiments.

The debonding damage that was observed in the 90-degree composite at a strain of 0.2 percent suggests that the radial bond strength is weak and probably negligible. In fact, our FEM analysis [Brust et al. (1991)] was able to predict the Poisson's ratio extremely well, assuming a zero bond strength. One way of evaluating the role of radial interface strength between the fiber and the matrix, is to determine the onset of Stage II at a higher temperature, where the effect of residual stresses is expected to be reduced. Figure 31 provides comparisons of the stress-strain curves at room temperature and 538 C. The three-stage deformation behavior is observed at both temperatures. However, more significant is that the onset of Stage II deformation occurs at a much lower stress at 538 C compared with that at room temperature. Thus, these results illustrate the dominant influence of residual stress on the inelastic deformation behavior of the 90-degree composite.

Additionally, from a design perspective, it may be prudent to base analyses on zero bond strength for this composite, because it would provide conservative assessment of local stresses and strains. We would also like to add, that strengths of ceramic-metal joints are often low (40-250MPa)[Majumdar and Ahmad (1991)], being generally lower than the typical stresses that are anticipated to be experienced by MMCs in service. Consequently, from an engineering standpoint, the assumption of zero bond strength may not be very

unrealistic.

The aspect of this work that we would like to emphasize is the understanding it provides about the mechanisms of inelastic deformation of MMCs. Observation of slip bands, aided by the fine ω -phase structure, provided useful information about the plasticity process. For the 0-degree composite, grain boundaries and reaction zones were important sources for dislocation nucleation. What was also interesting was that although the reaction-zone cracks started appearing at strains as low as 0.3 percent, slip band activity had to wait until the matrix stress in the bulk was close to the yield strength of the matrix material. We believe that this was so because the reaction-zone cracks were small, having stress intensity factors in the range 1 to 4 MPa $\sqrt{\text{m}}$. However, the characteristics of the fiber-matrix interface, coupled with constraints offered by the surrounding fiber and matrix, also probably contributed in delaying slip band activity at reaction zone cracks, in the highly thermally-stressed region surrounding the fiber.

Regarding the 90-degree composite, the experiments indicated that the radial fiber-matrix bond for the composite is low, which was responsible for the propensity for debonding. A stronger interface strength is certainly desired. In Stage II, plasticity was also observed, in addition to debonding. The initial slip bands nucleated primarily from reaction-zone cracks. It appears that these cracks were, in turn, caused by preliminary debonding, for only then could sufficient tangential stress be generated to cause cracking of the reaction zone.

The intense shear bands that were observed in Stage II probably were influenced by the staggered arrangement of fibers in adjacent plies. As already indicated, such an arrangement may be a result of the processing history. Further work is needed to clarify and establish this point. The occurrence of intense shear bands likely was responsible for the stress-strain curve becoming almost flat in Stage III. Additionally, they hastened the nucleation of shear cracks from reaction-zone cracks, and their ultimate propagation to shear-dominated failure. This mechanism most likely was responsible for significantly reducing the elongation to failure of the composite (< 2 percent) compared with the matrix material.

Figures 32 and 33 summarize our current understanding of the sequence of events

associated with the deformation of 0-degree and 90-degree MMCs. These figures are based on the measurements and mechanisms observed in this investigation. They indicate that both plasticity and damage must be incorporated in any comprehensive model of MMCs. Additionally, models must include the effect of reaction zones and the processing histories. To our knowledge, extremely little attention has been focussed on these aspects of the problem in modeling studies.

7. CONCLUSIONS

The following conclusions may be drawn based on the work presented here:

- (i) Inelastic deformation of the 0-degree MMC is dominated by plasticity at room temperature. This was confirmed by a combination of mechanical measurements and metallurgical evaluation techniques.
- (ii) The sequence of events associated with inelastic deformation of the 0-degree composite has been identified.
- (iii) The 90-degree composite has a characteristic three-stage deformation behavior: Stages I, II, and III. The width Poisson's ratios show an intermediate plateau behavior in Stage II, with the ratio decreasing to zero in Stage III.
- (iv) Inelastic deformation of the 90-degree composite is controlled by both damage and plasticity, and the sequence of events associated with the inelastic deformation response has been identified.
- (v) The existence of a fine coherent ω -phase in the as-processed Ti 15-3 matrix of the composite material likely was responsible for observation of concentrated slip and dislocation pileup type of configurations.
- (vi) Residual stresses play a key role in the debonding of the 90-degree composite. Thus, whereas residual stresses may be undesirable for the 0-degree MMC, they may be desirable for the 90-degree MMC.

- (vii) Formation of intense shear bands in Stage III (for the 90-degree composite), and their influence in hastening shear dominated failure, likely were responsible for low elongation to failure of the 90-degree composite compared with the matrix material.
- (viii) Comparisons of the experimental results with the predictions of an elastic-plastic model show that rigorous validation is necessary to establish whether a model is adequate for predicting the constitutive response of a MMC.

8. ACKNOWLEDGEMENTS

This work was supported by the NASA-Lewis Research Center, under contract number NAS3-26053 through the HITEMP program. We specially thank our monitor, Dr. J. Rod Ellis of NASA Lewis, for his constant encouragement and guidance throughout this program. We would also like to acknowledge the many useful discussions with Drs. B. Lerch and M. Castelli of NASA Lewis, and the data they provided for use in this work. We thank Dr. F.W. Brust of Battelle for providing preliminary results of the elastic-plastic-damage FEM analysis. Finally, we thank Mr. N. Frey, Mr. G. Foster and Mr. G. Clark of Battelle and Mr. Hendrick Coljin of Ohio State University for their excellent experimental support during this program.

9. REFERENCES

- ABOUDI, J., 1984 *Int. J. Engng. Sci.* **22**, 439-449
- ADAMS, D.F., 1970 *J. Comp. Mater.* **7**, 310-328
- ADAMS, D.F. and DONER, D.R., 1967, *J. Comp. Mater.* **1**, 4
- BLACKBURN, M.J., and WILLIAMS, J.C., 1968, *Trans. Metall. Soc. AIME*, **242**, 2461
- BRUST, F.W., NEWAZ, G.M., and MAJUMDAR, B.S., 1991, to be presented at the 1992 ASTM Spring Symposium
- CHAMIS, C.C. and HOPKINS, D.A., 1988 *Testing Technology of Metal Matrix Composites*, Ed. P.R. Giovanni and N.R. Adsit, ASTM STP 964, 177-196
- DVORAK, G.J. and BAHEI-EL-DIN, Y.A., 1982 *J. Appl. Mech.* **49**, 327-335
- HAMILTON, C.H., HECKER, S.S., and EBERT, L.J. 1971, *J. of Basic Engng.*, Trans. ASME, 661-671
- HASHIN, Z. and ROSEN, B.W., 1964 *J. Appl. Mech.* **31E**, 223
- HASHIN, Z., 1979, *J. Appl. Mech.* **46**, 543
- HILL, R. 1964, *J. Mech. Phys. Solids* **12**, 213-218
- JOHNSON, W.S., LUBOWINSKI, S.J., BREWER, W.D., and HOOGSTRATEN, C.A., 1988, *Mechanical Characterization of SCS6/Ti 15-3 Metal Matrix Composites at Room Temperature*, NASP Technical Memorandum 1014, NASA Langley Research Center
- KELLY, A. and TYSON, W.R., 1965 *J. Mech. Phys. Solids* **13**, 329
- KELLY, A., 1972 *Metall. Trans.* **3**, 2313
- LERCH, B.A., and SALTSMAN, J., 1991, *Tensile Deformation Damage in SiC Reinforced Ti-15V-3Cr-3Al-3Sn*, NASA Technical Memorandum 103620, NASA Lewis Research Center
- MAJUMDAR, B.S. and NEWAZ, G.M. 1991, *Third International Symposium on Composite Materials*, Ed. K. O'Brien, ASTM STP1110
- MAJUMDAR, B.S., and NEWAZ, G.M., and ELLIS, J.R. 1991 to be submitted to *Metall. Trans.*
- MAJUMDAR, B.S. and AHMAD, J.A. 1991, *Metal-Ceramic Joints*, Ed. P. Kumar, Proc. of TMS Symposium held in Detroit in October 1990
- McCABE, K.K., and SASS, S.L., 1971, *Phil. Mag.*, **23**, 957-970

- MOREL, M., SARAVANOS, D.A., and CHAMIS, C.C. 1990, *Concurrent Micromechanical Tailoring and Fabrication Process Optimization for Metal-Matrix Composites*, NASA Technical Memorandum 103670, NASA Lewis Research Center
- NEWAZ, G.M., and MAJUMDAR, B.S. 1991, to be presented at the ASME Winter Meeting and to be published as ASME AD Volume
- NEWAZ, G.M., MAJUMDAR, B.S., and BRUST, F.W., 1991 *J. Eng. Mat. and Tech.*, ASME, in press.
- NIMMER, R.P., BANKERT, R.J., RUSSELL, E.S., SMITH, G.A., and WRIGHT, K.P., 1991, *J. Composite Technology and Research*, **13**, 1, 3-13
- PINDER, M.J. and LIN, M.W., 1989 *J. Pressure Vessel Tech.* Trans. ASME **111**, 183-190
- ROBINSON, D.N., DUFFY, S.F. and ELLIS, J.R., 1987, *Thermal Stress, Material Deformation and Thermo-Mechanical Fatigue*, Ed. H. Sehitoglu and S.Y. Zamrik, ASME-PVP, Vol.123, 49-56
- SASS, S.L., 1969, *Acta Metall.*, **17**, 813-820
- SILCOCK, J.M., 1958, *Acta Metall.*, **6**, 48
- SUN, C.T. 1989, *Metal Matrix Composites*, Ed. W.S. Johnson, *ASTM STP 1032*, 148-160
- WALKER, K.P., JORDAN, E.H., and FREED, A.D. 1989, *Nonlinear mesomechanics of Composites with Periodic Microstructure: First Report*, NASA Technical Memorandum **102051**, NASA Lewis Research Center, Cleveland, Ohio, USA

LIST OF FIGURES

- Figure 1. Schematic illustrating compliance changes associated with plasticity and damage.
- Figure 2. Schematic illustrating effects of plasticity and damage on the Poisson's ratio.
- Figure 3. Schematic showing definitions of the longitudinal, width, and thickness strains.
- Figure 4. Stress versus longitudinal strain for 0-degree Ti 15-3/SCS6 composites.
- Figure 5. Width strain plotted versus the longitudinal strain for the 0-degree Ti 15-3/SCS6 composite.
- Figure 6. Thickness strain plotted versus the longitudinal strain for the 0-degree Ti 15-3/SCS6 composite.
- Figure 7. Stress versus the longitudinal strain for 90-degree Ti 15-3/SCS6 specimens.
- Figure 8. Width strain plotted versus the longitudinal strain for the 90-degree Ti 15-3/SCS6 composite.
- Figure 9. Total thickness Poisson's ratio plotted versus the longitudinal strain for the 90-degree Ti 15-3/SCS6 composite.
- Figure 10. Stress versus longitudinal strain for the Ti 15-3 matrix material obtained by foil consolidation.
- Figure 11. (a) Longitudinal, and, (b) transverse cross sections of the as-received Ti 15-3/SCS6 composite; as-polished sample. A,B, and C correspond to the fiber, reaction-zone, and matrix, respectively.
- Figure 12. (a) Longitudinal, and, (b) transverse cross sections of the as-received Ti 15-3/SCS6 composite; polished and etched sample. The arrow (gb) shows a grain-boundary.
- Figure 13. Etched microstructure of the surface of a 0-degree Ti 15-3/SCS6 composite, unloaded from a total strain of 0.9 percent. The slip bands (sb), indicated by arrows, may be seen emanating from grain boundaries. Loading axis is vertical.
- Figure 14. Etched microstructures of a 0-degree Ti 15-3/SCS6 composite, unloaded from a total strain of 0.9 percent. The specimen has been polished down to the first set of fibers. Large slip band (sb) activity confirms plasticity in the MMC. Loading axis is along fiber direction.

- Figure 15. (a) Higher magnification optical micrograph, corresponding to Figure 14, showing slip bands (sb) associated with reaction-zone cracks; (b) SEM micrograph of another region, showing slip bands (sb) emanating from the reaction-zone/matrix interface.
- Figure 16. Longitudinal cross section of a 0-degree specimen, showing fiber and Mo-ribbon fractures associated with failure of the composite. The region next to the fracture surface is shown in (a). The region in (b) is approximately 5 mm from the fracture surface, showing cracking of fibers and Mo-ribbon at that location.
- Figure 17. TEM micrograph of the as-received material, showing built-in dislocation structures.
- Figure 18. TEM micrograph of the as-received material, showing built-in dislocation structures.
- Figure 19. TEM micrographs of the deformed 0-Degree Ti 15-3/SCS6 composite. Images taken around the $[011]$ zone axis. (a) Bright field, and (b) Dark field.
- Figure 20. TEM micrographs of the deformed 0-Degree Ti 15-3/SCS6 composite, showing intersecting slip bands.
- Figure 21. Series of four selected area diffraction patterns (SADP) showing streaking associated with the extremely fine ω -phase (hcp) in the β (bcc) matrix. (a) $\mathbf{B} - (110)_{\beta}$, (b) $\mathbf{B} - (111)_{\beta}$, (c) $\mathbf{B} - (120)_{\beta}$ and (d) $\mathbf{B} - (331)_{\beta}$. The directions of the streaks in each SADP were determined to be in agreement with the ω -phase being distributed in rows along the $\langle 111 \rangle_{\beta} \parallel \langle 0001 \rangle_{\omega}$ direction. The points a, b, and c in (c) correspond to $(\bar{1}011)$, $(\bar{2}020)$ and (0001) reflections of the ω -phase.
- Figure 22. Optical micrographs of the edge cross-section of a 90-degree composite, strained to approximately 1.6 percent (Stage III); as-polished sample, and the loading axis is vertical. The higher magnification micrograph (b) illustrates both debonding and cracking of the reaction zone.
- Figure 23. Longitudinal section of a 90-degree composite deformed into Stage III. Debonding and cracking at the fiber-matrix interface is shown by an arrow.
- Figure 24. Etched microstructure of a 90-degree specimen, loaded into Stage III. Two types of slip band activity are indicated by regions A and B. Final failure of

the composite occurred by crack initiation and failure along the intense shear bands.

- Figure 25. Optical photomicrograph of a 90-degree specimen, unloaded from a strain of 0.5 percent (Stage II). The slip bands (white lines) are mostly associated with reaction-zone cracks; the latter, although faint in this figure, are indicated by arrows. Loading axis is vertical.
- Figure 26. Surface replica of a 90-degree specimen strained to 0.3 percent (the beginning part of Stage II); replica taken at full load. The region indicated by arrow corresponds to the acetate tape entering into the debonded fiber-matrix interface. The loading axis is vertical.
- Figure 27. Replica of the same region as Figure 26, after the load had been reduced to zero. There is no acetate tape protruding, indicating that the fiber-matrix separation has largely closed upon unloading.
- Figure 28. Comparison of model predictions with experimental data for the 0-degree Ti 15-3/SCS6 composite.
- Figure 29. Comparison of model predictions with experimental data for the 90-degree Ti 15-3/SCS6 composite.
- Figure 30. Comparison of model predictions with experimental data for the 90-degree Ti 15-3/SCS6 composite.
- Figure 31. Plot showing effects of temperature on the stress versus longitudinal strain response for the 90-degree composite.
- Figure 32. Deformation sequence for the 0-degree composite, based on current observations.
- Figure 33. Deformation sequence for the 90-degree composite, based on current observations.

TABLE 1. Special Characteristics of Plasticity and Damage

Characteristic	Plasticity	Damage
Specimen compliance	Unchanged with plasticity	Increases with damage
Strain offset at zero load	Positive strain offset	Zero strain offset
Poisson's ratio	Increases in going from the elastic into the plastic regime of deformation	Decreases in going from the elastic into the damage regime of deformation
Cracks and debonding	No	Yes
Changes in dislocation density and configuration in the bulk	Yes	No

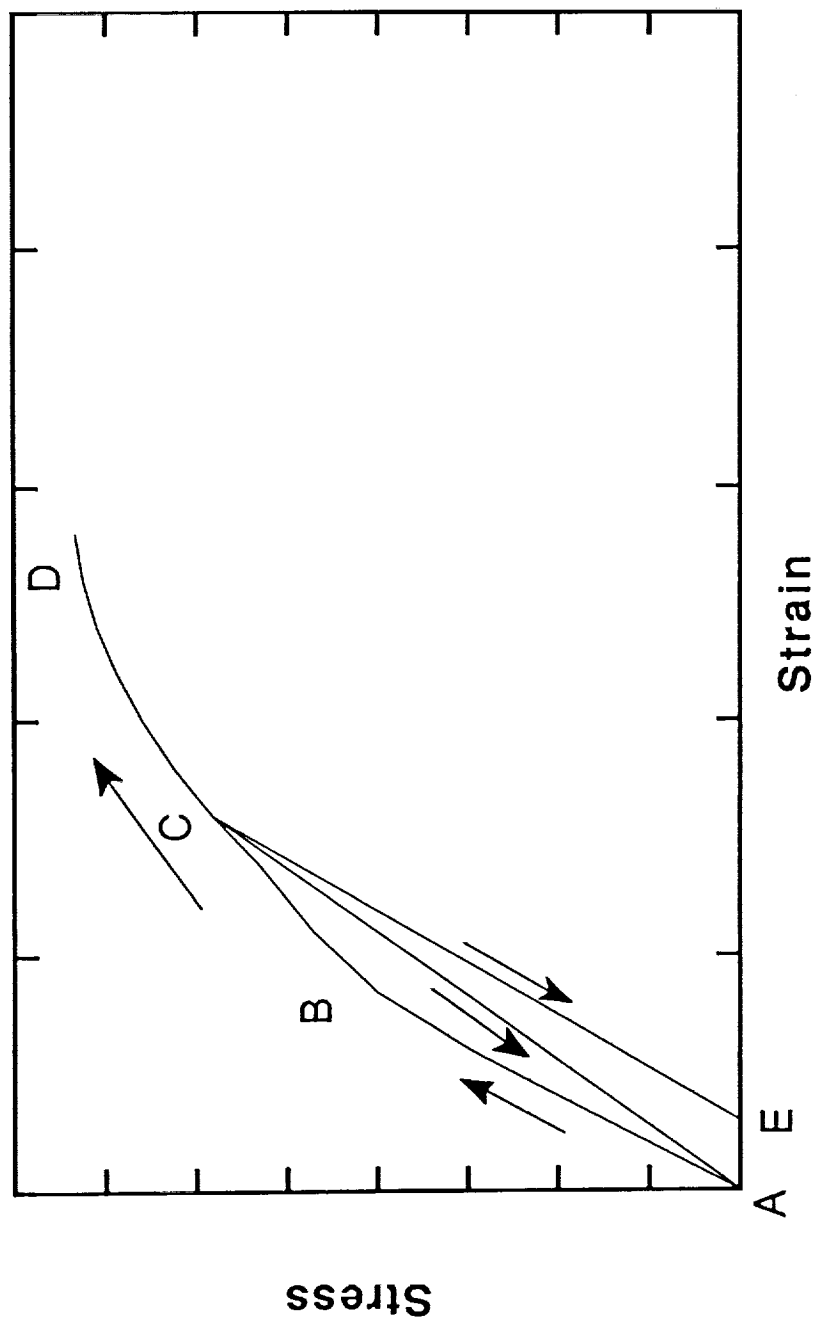


Figure 1. Schematic Illustrating Compliance Changes Associated with Plasticity and Damage

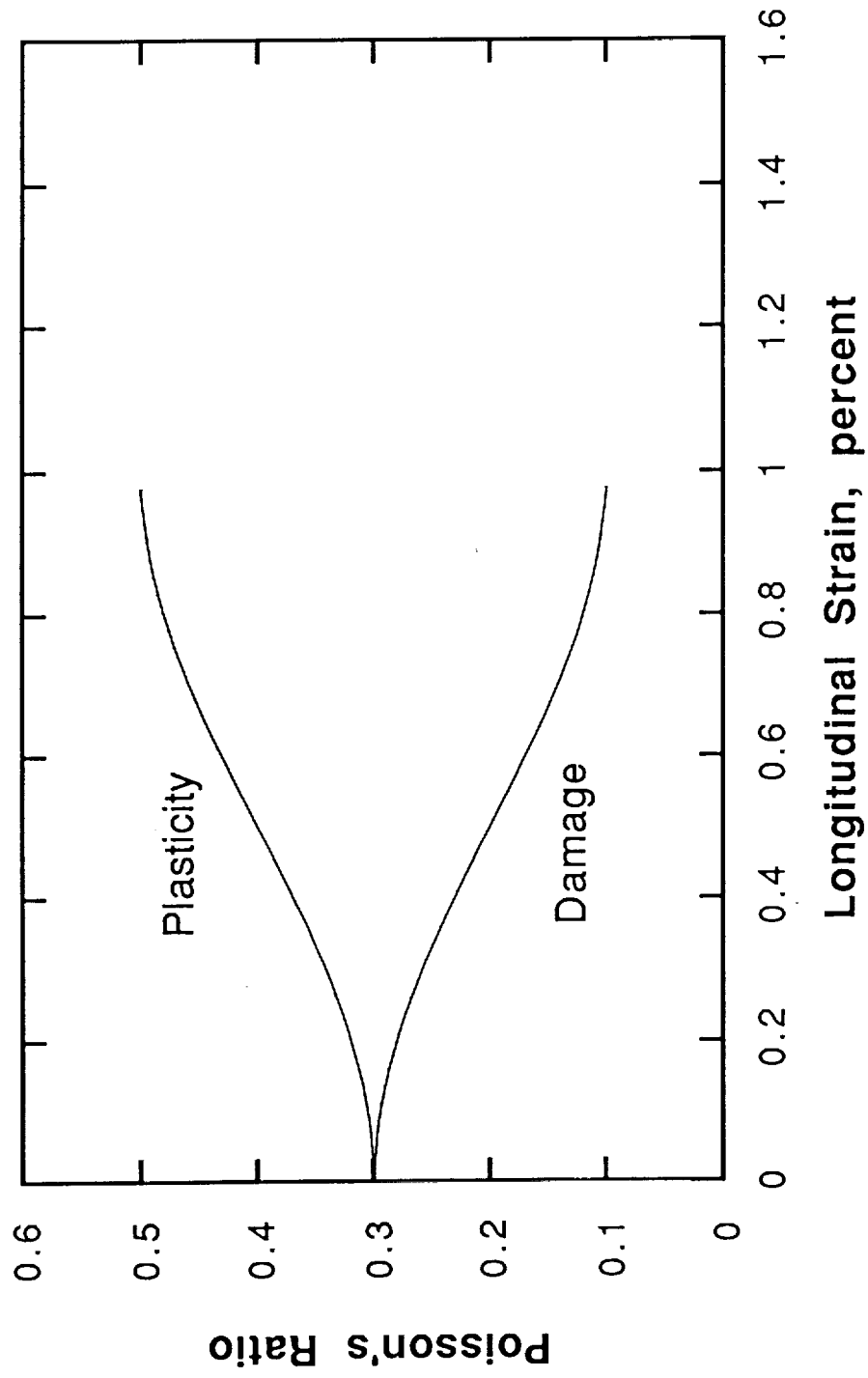


Figure 2. Schematic Illustrating Effects of Plasticity and Damage on the Poisson's Ratio

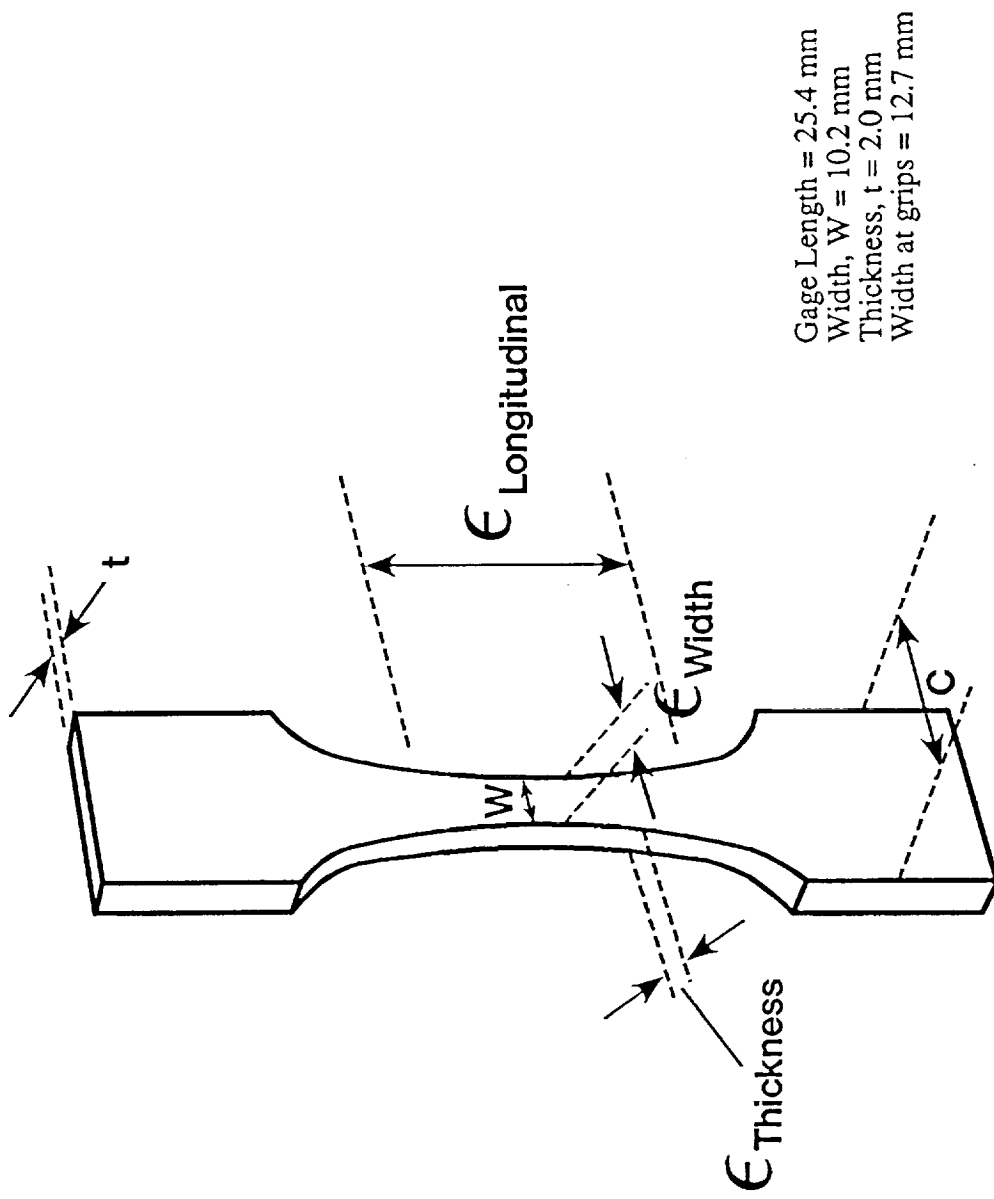
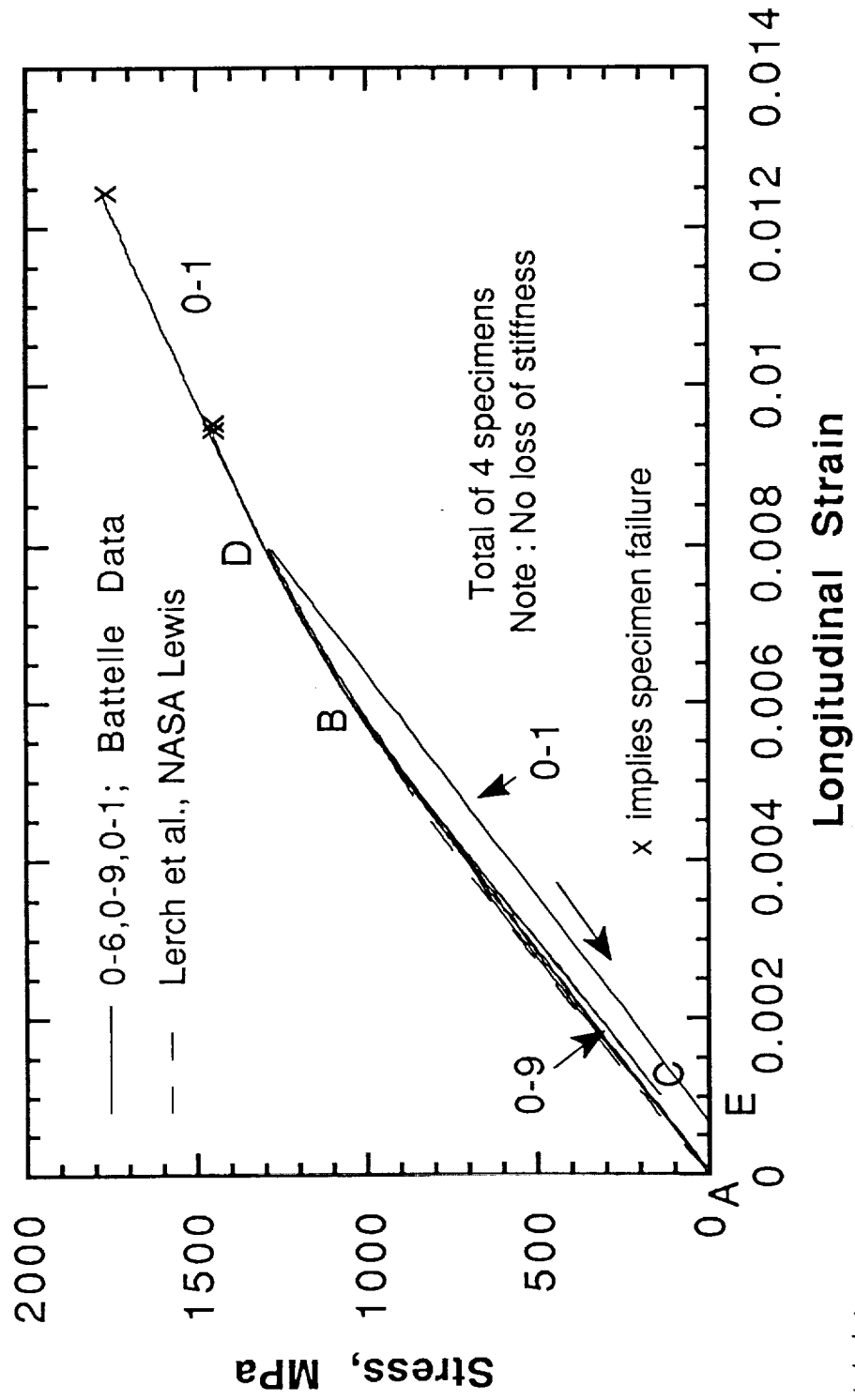
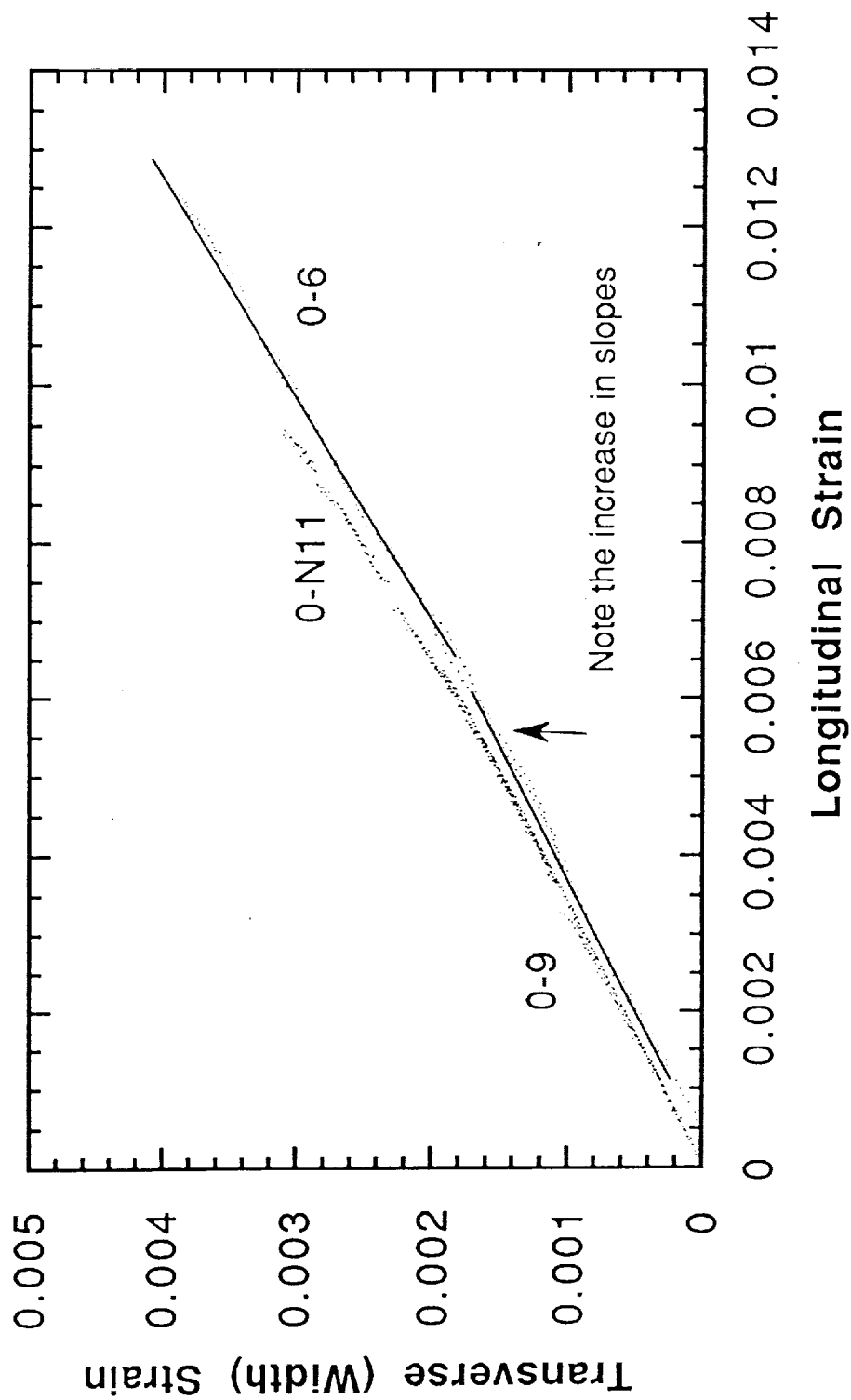


Figure 3. Schematic showing definitions of the longitudinal, width, and thickness strains.



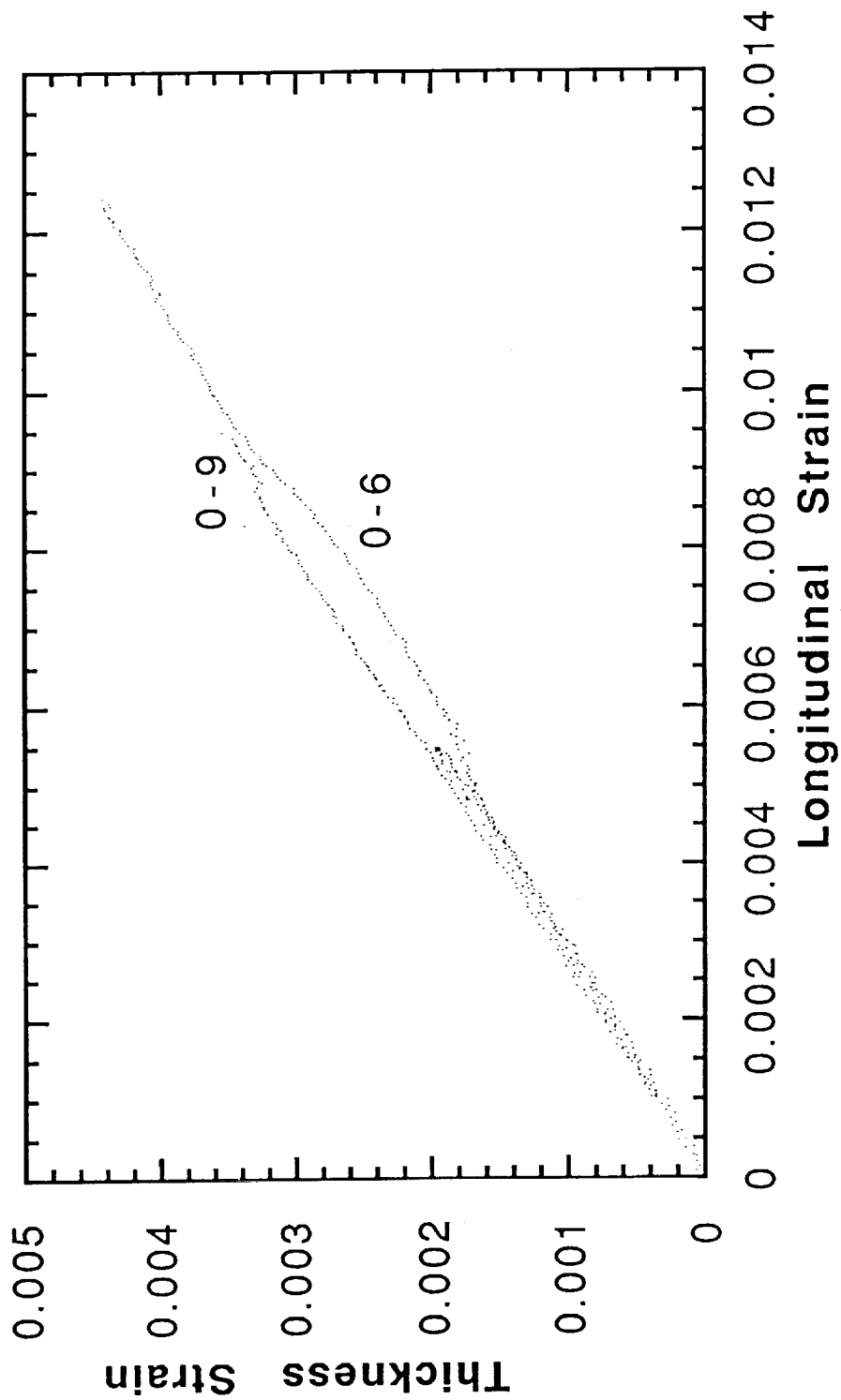
06090n1nl.plot

Figure 4. Stress Versus Longitudinal Strain for 0-Degree TI 15-3/SCS6 Composites



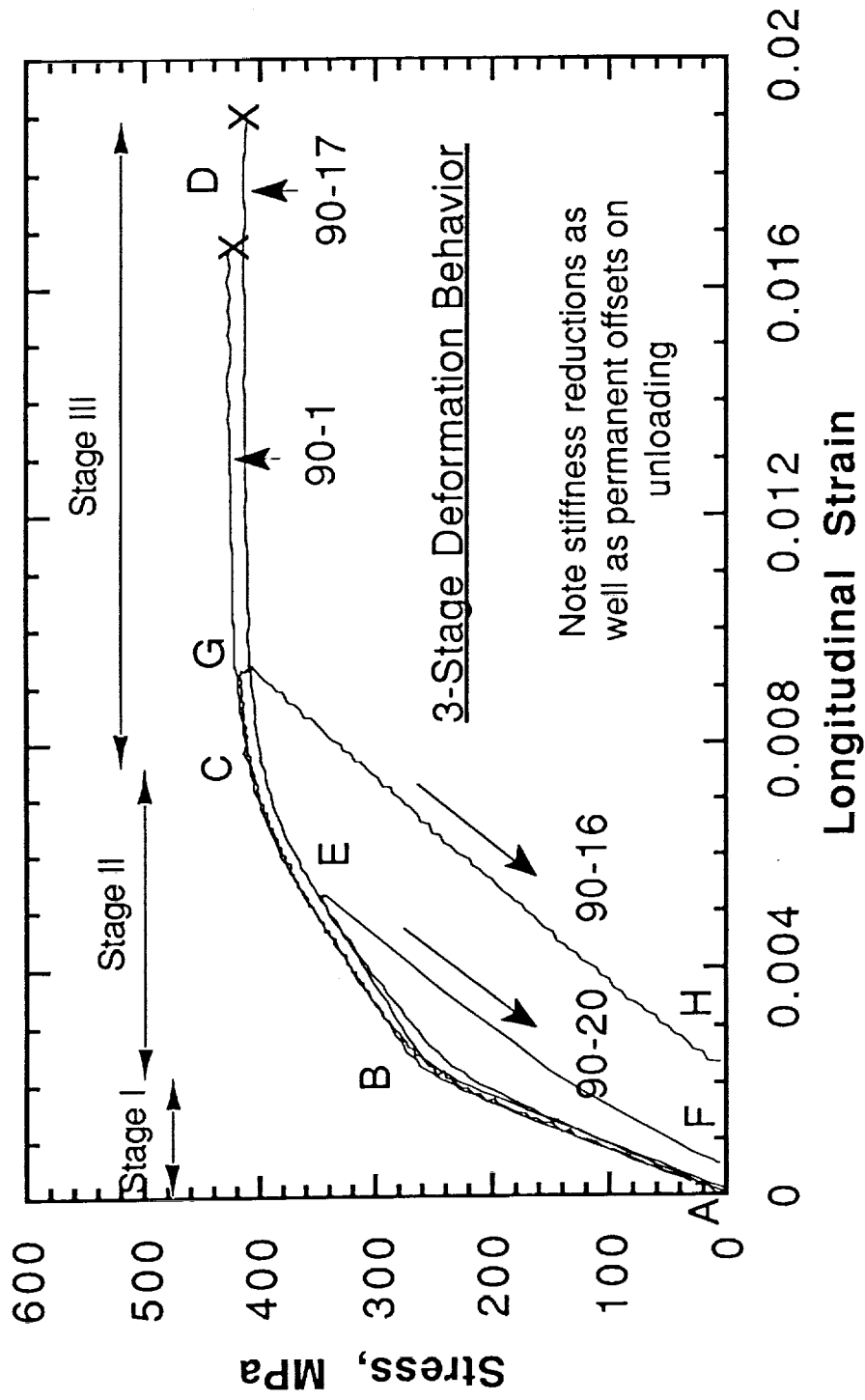
06090n11wvsl.plot

Figure 5. Width Strain Plotted Versus the Longitudinal Strain for the 0-Degree Ti 15-3/SCS6 Composite



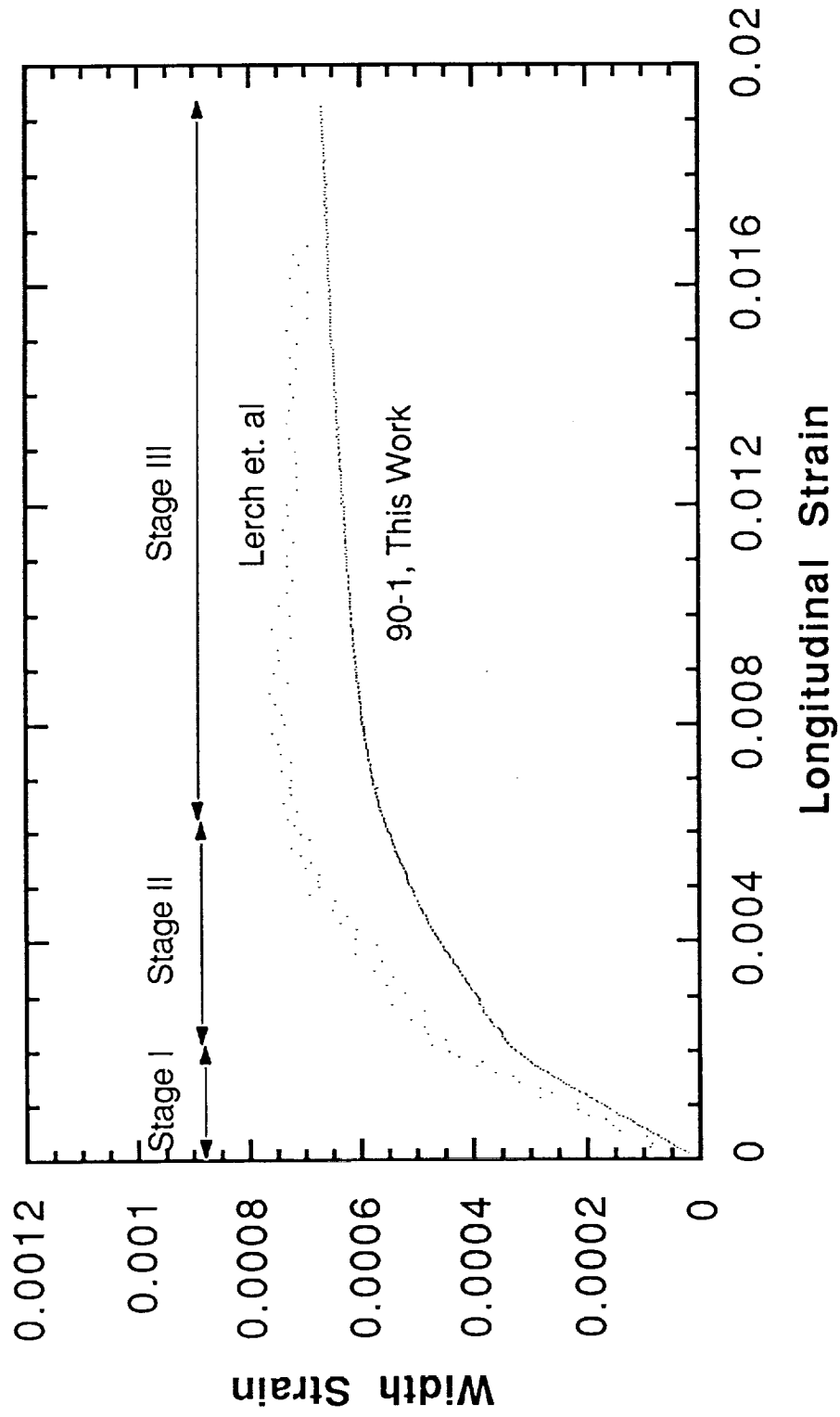
0609tsvsls.plot

Figure 6. Thickness Strain Plotted Versus the Longitudinal Strain for the 0-Degree TI 15-3/SCS6 Composite



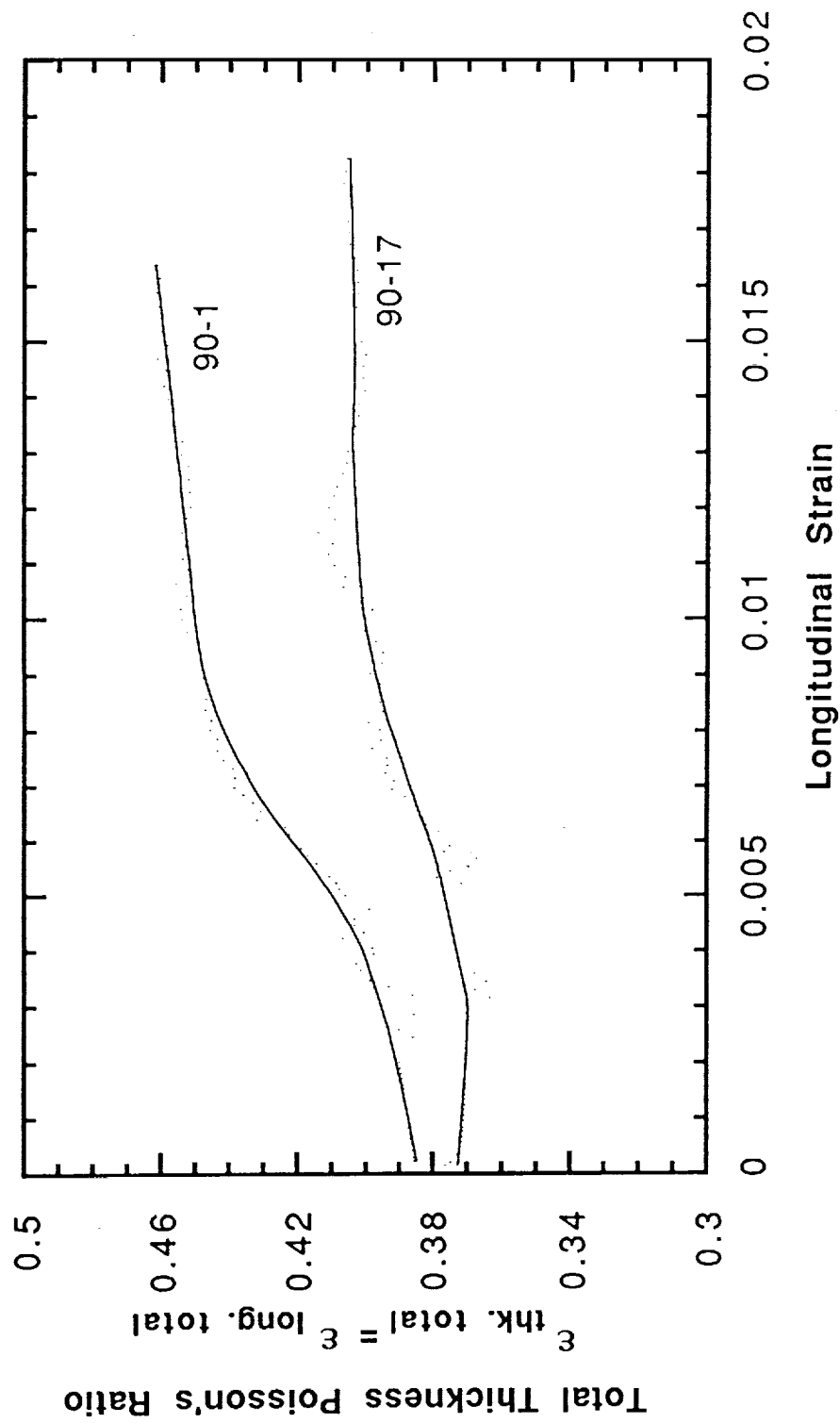
901901790209016stvs1s.plot2

Figure 7. Stress Versus the Longitudinal Strain for 90-Degree Ti 15-3/SCS6 Specimens



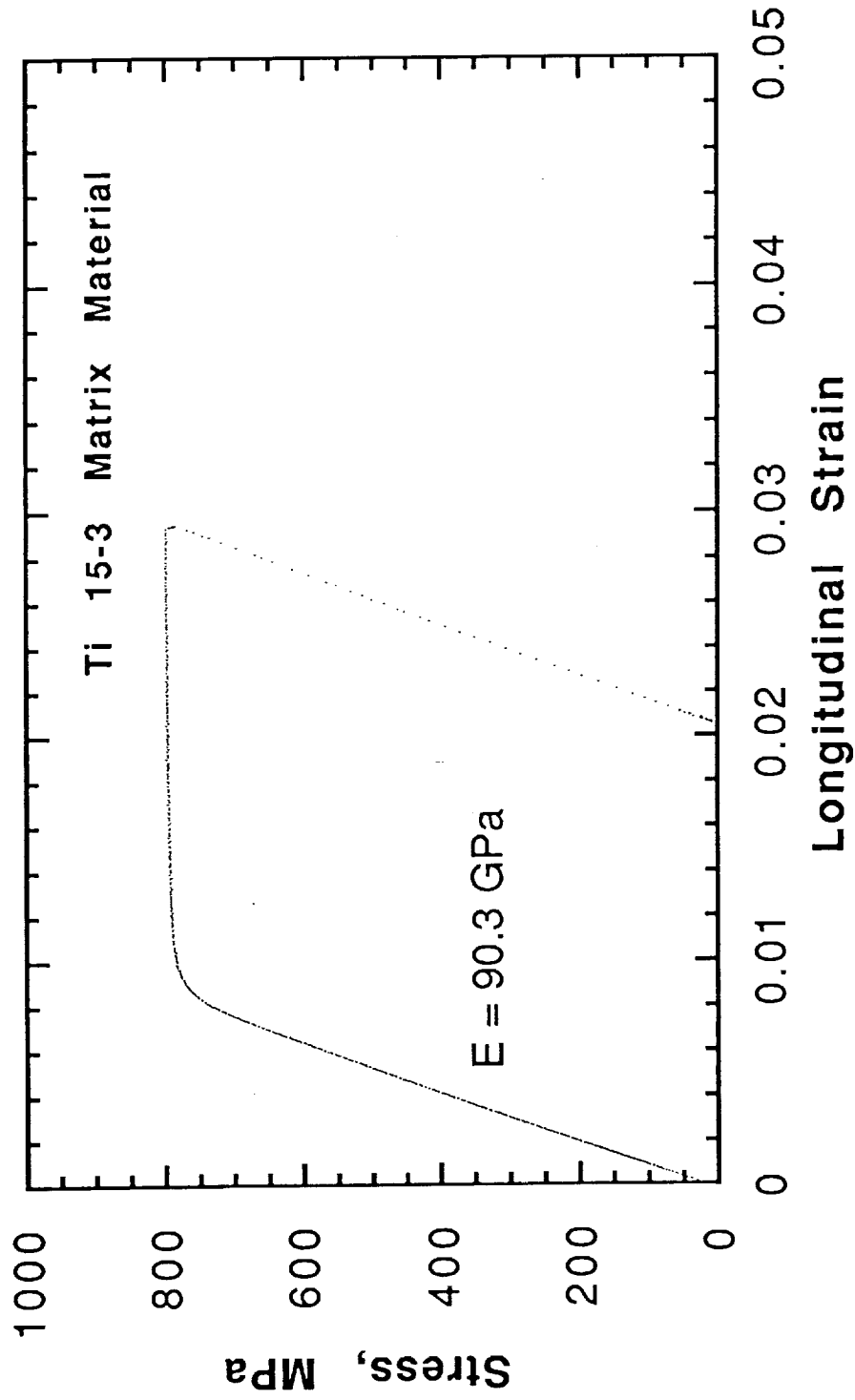
90190nlwsvsls.plot

Figure 8. Width Strain Plotted Versus the Longitudinal Strain for the 90-Degree Ti 15-3/SCS6 Composite



9019017tottsmvsls.plot

Figure 9. Total Thickness Poisson's Ratio Plotted Versus the Longitudinal Strain for the 90-Degree Ti 15-3/SCS6 Composite



m11stvs/s.plot

Figure 10. Stress Versus Longitudinal Strain for the Ti 15-3 Matrix Material Obtained by Foil Consolidation

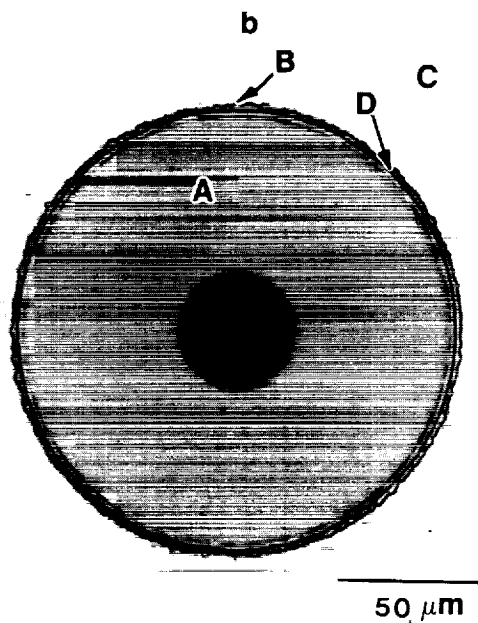
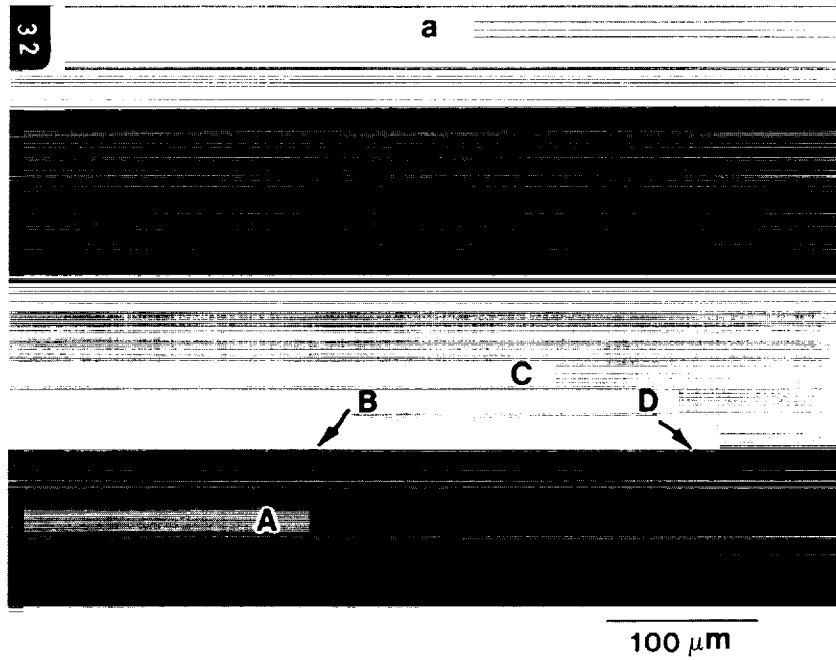


Figure 11. (a) Longitudinal, and, (b) transverse cross sections of the as-received Ti 15-3/SCS6 composite; as-polished sample. A,B, and C correspond to the fiber, reaction-zone, and matrix, respectively.

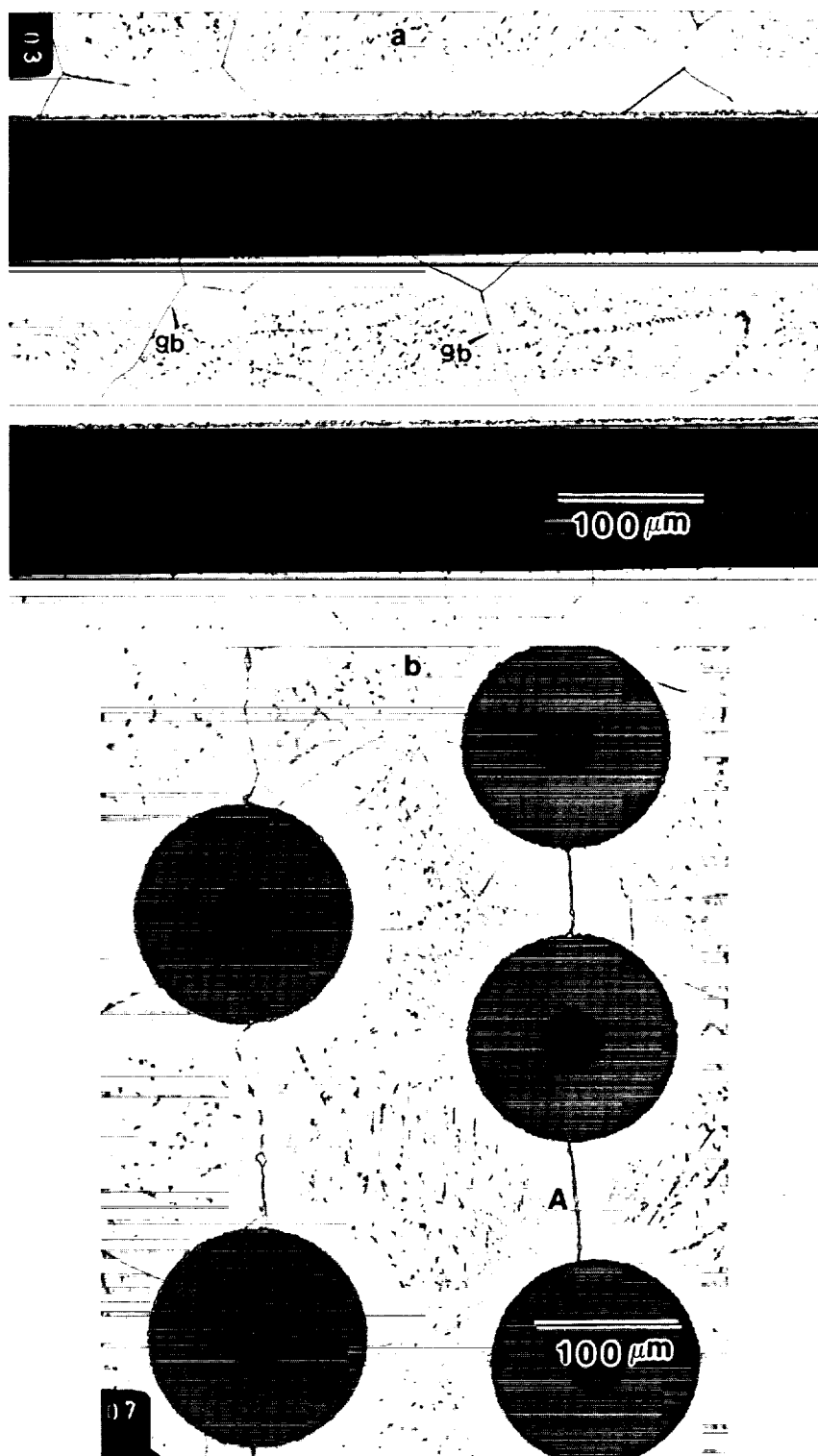


Figure 12. (a) Longitudinal, and, (b) transverse cross sections of the as-received Ti 15-3/SCS6 composite; polished and etched sample. The arrow shows a grain-boundary.

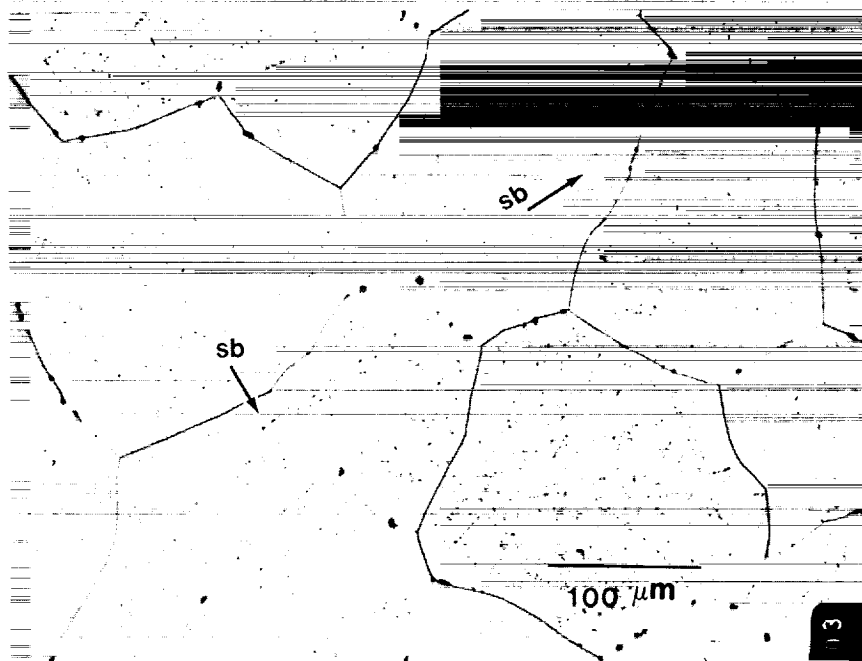


Figure 13. Etched microstructure of the surface of a 0-degree Ti 15-3/SCS6 composite, unloaded from a total strain of 0.9 percent. The slip bands (indicated by arrows) may be seen emanating from grain boundaries.

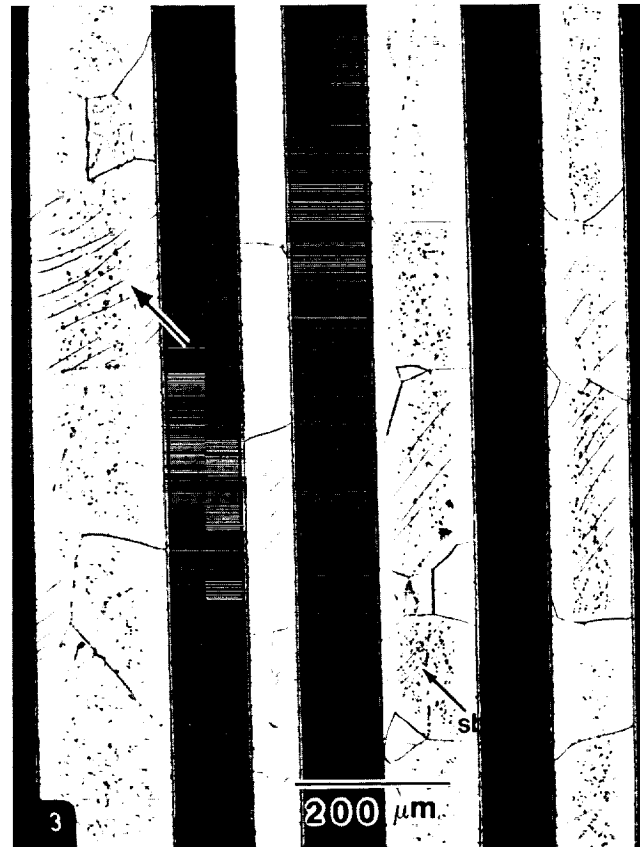


Figure 14. Etched microstructures of a 0-degree Ti 15-3/SCS6 composite, unloaded from a total strain of 0.9 percent. The specimen has been polished down to the first set of fibers. Large slip band activity confirms plasticity in the MMC.

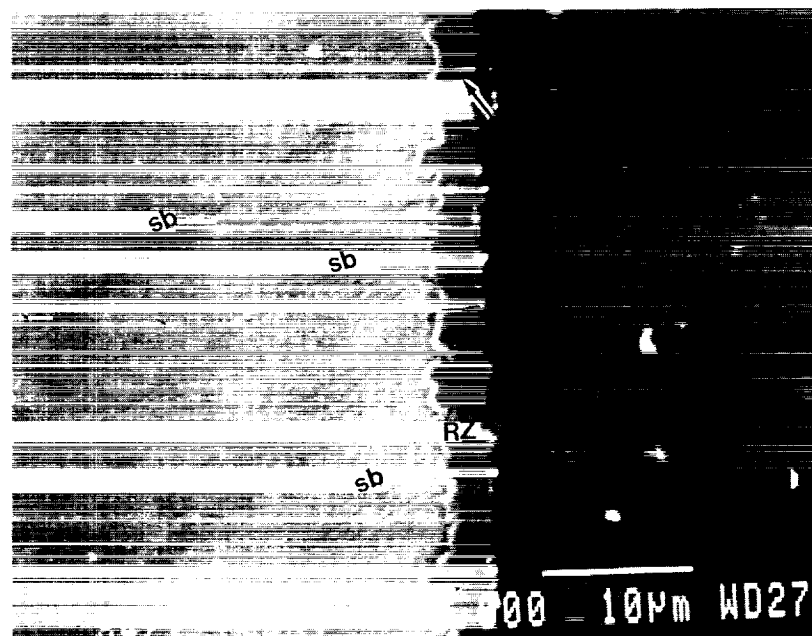
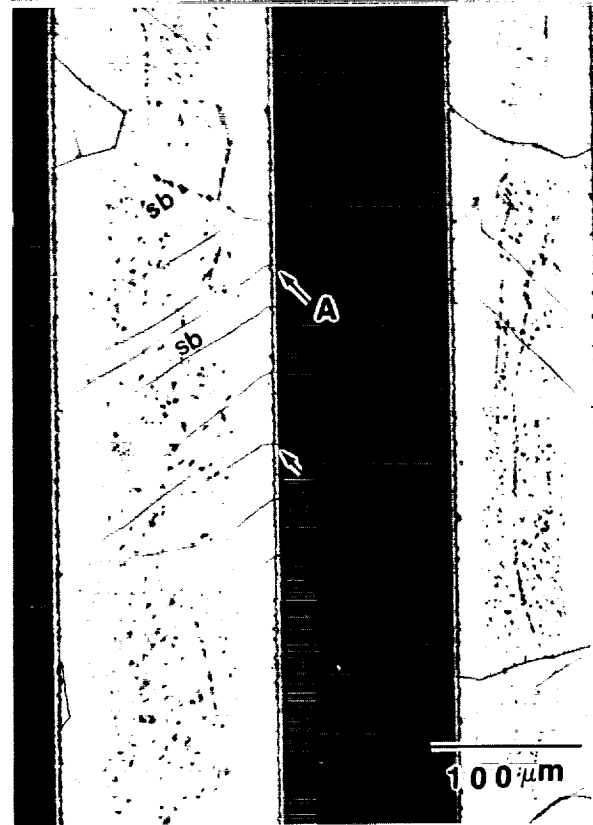


Figure 15. (a) Higher magnification optical micrograph, corresponding to Figure 14, showing slip bands associated with reaction-zone cracks; (b) SEM micrograph of another region, showing slip bands emanating from the reaction-zone/matrix interface.

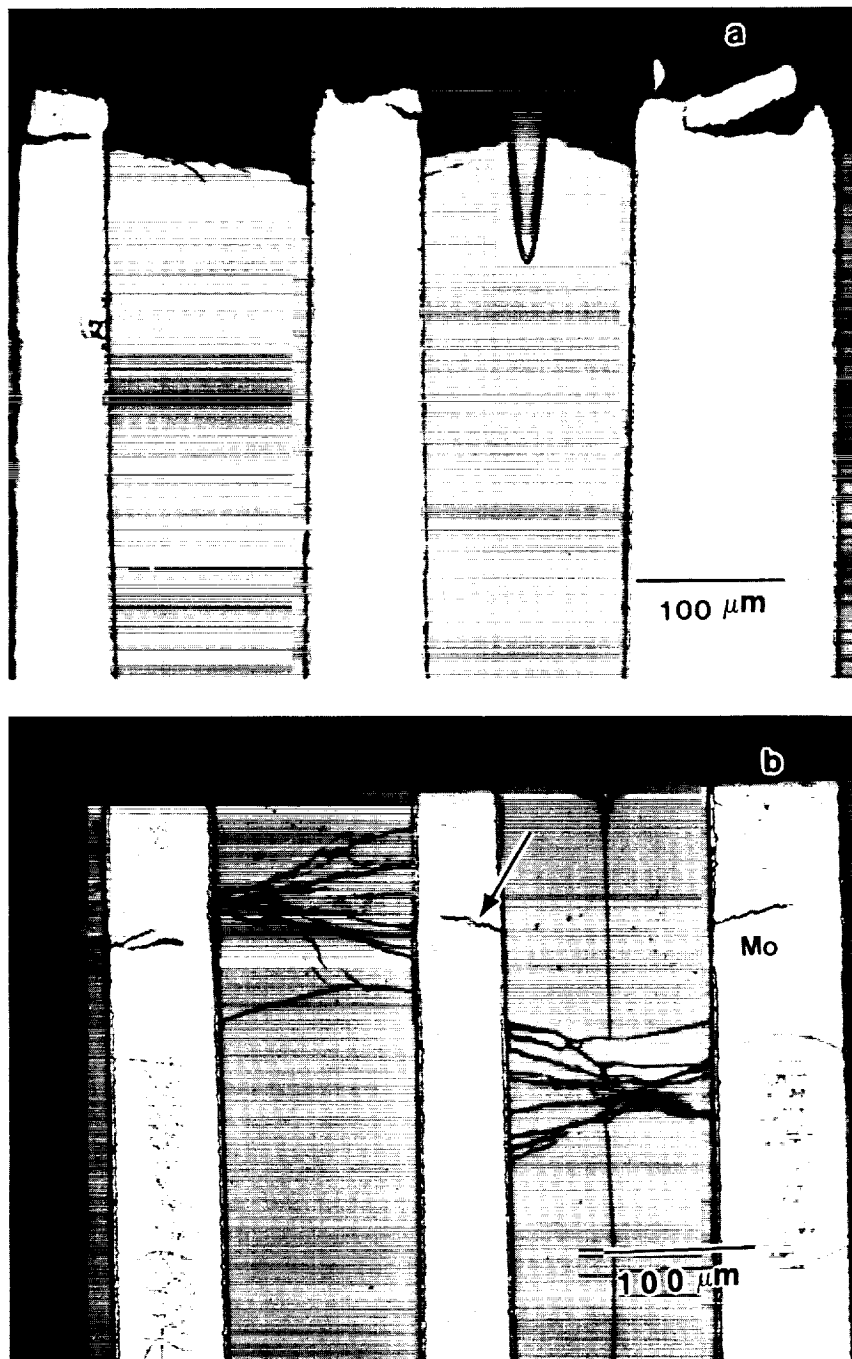


Figure 16. Longitudinal cross section of a 0-degree specimen, showing fiber and Mo-ribbon fractures associated with failure of the composite. The region next to the fracture surface is shown in (a). The region in (b) is approximately 5 mm from the fracture surface, showing cracking of fibers and Mo-ribbon at that location.

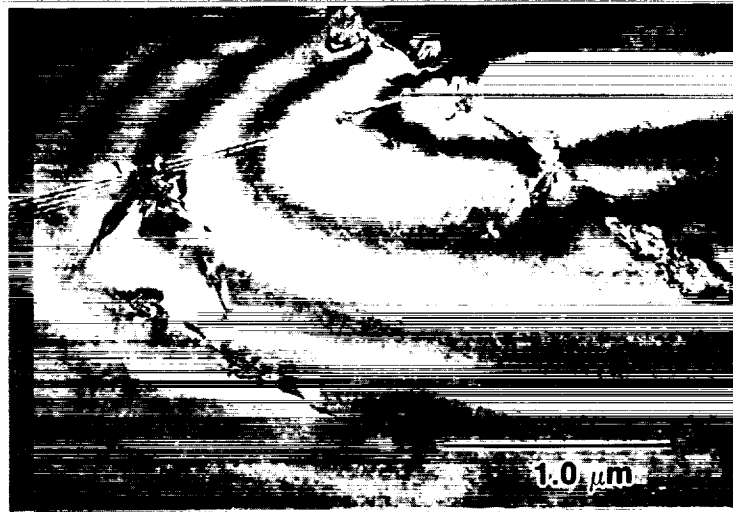


Figure 17. TEM micrograph of the as-received material, showing built-in dislocation structures.

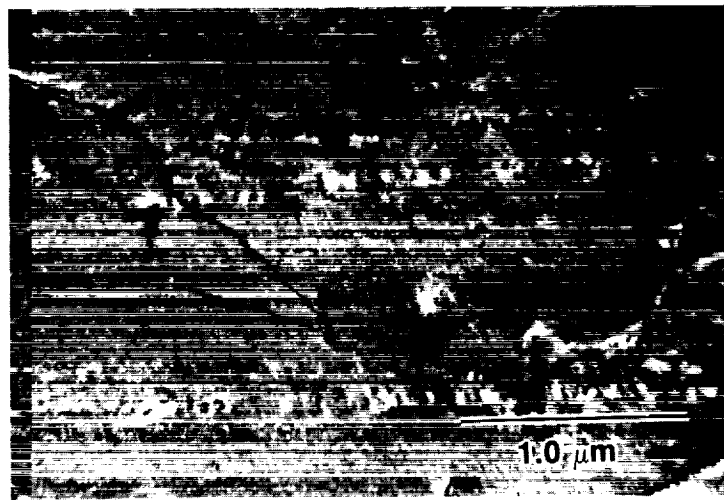


Figure 18. TEM micrograph of the as-received material, showing built-in dislocation structures.

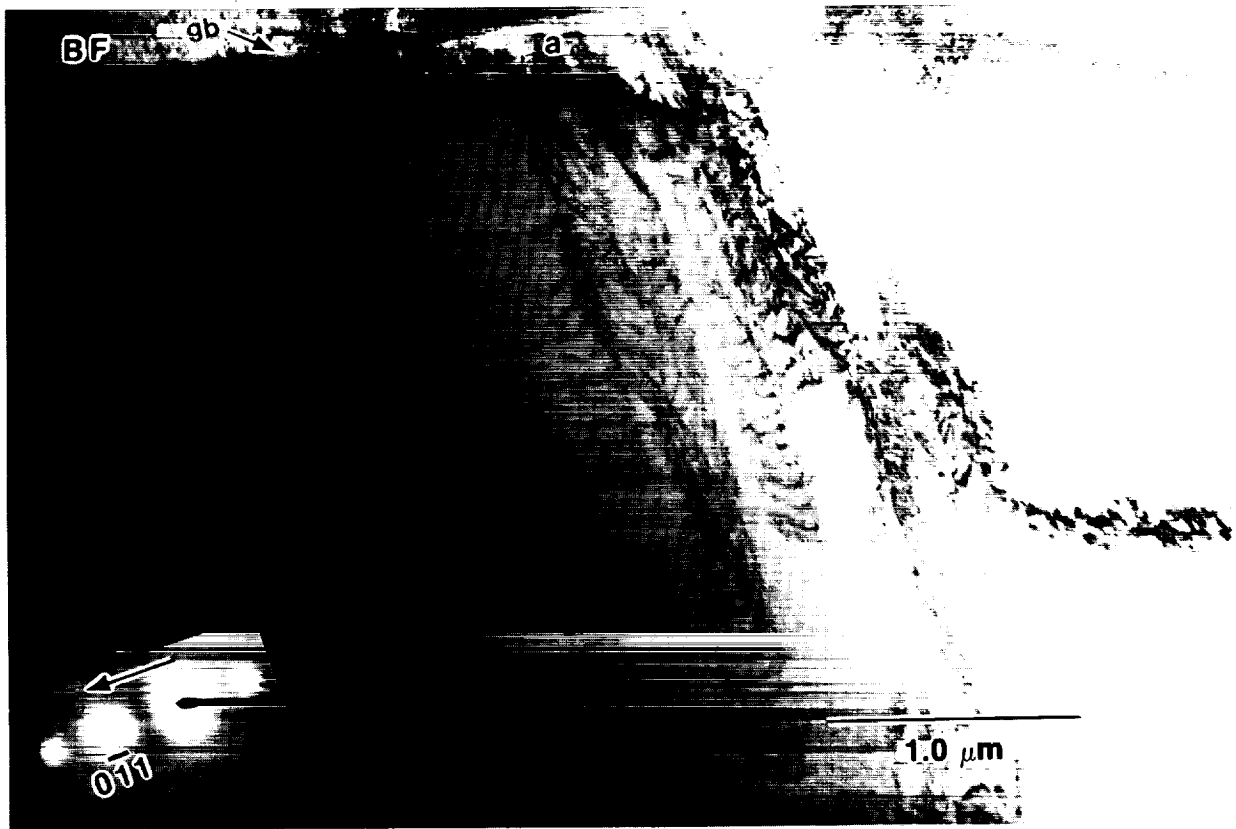


Figure 19. TEM micrographs of the deformed 0-Degree Ti 15-3/SCS6 composite. Images taken around the [011] zone axis. (a) Bright field, and (b) Dark field.



Figure 19. TEM micrographs of the deformed 0-degree Ti 15-3/SCS6 composite. Images taken around the $[011]$ zone axis. (a) Bright field, and (b) Dark field.

ORIGINAL PAGE
BLACK AND WHITE PHOTOGRAPH

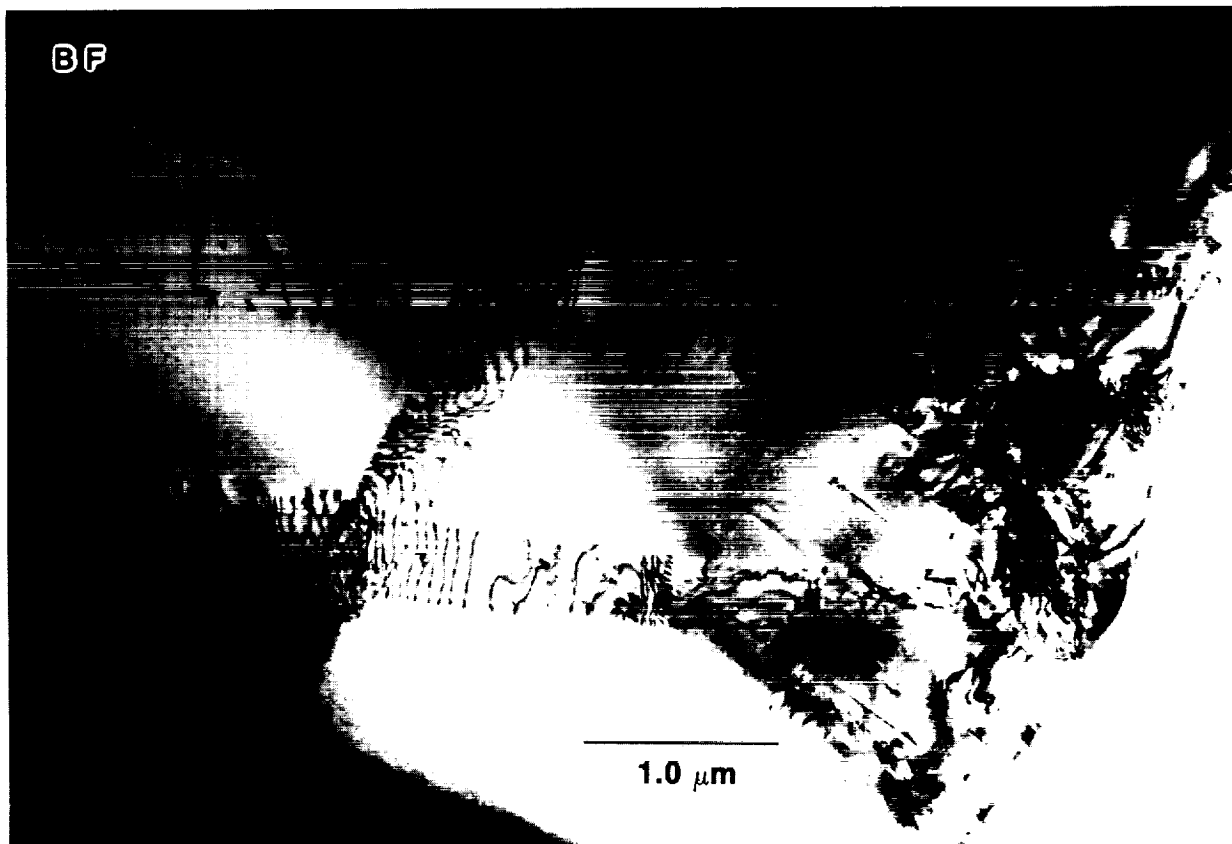


Figure 20. TEM micrographs of the deformed 0-Degree Ti 15-3/SCS6 composite, showing intersecting slip bands.

ORIGINAL PAGE
BLACK AND WHITE PHOTOGRAPH

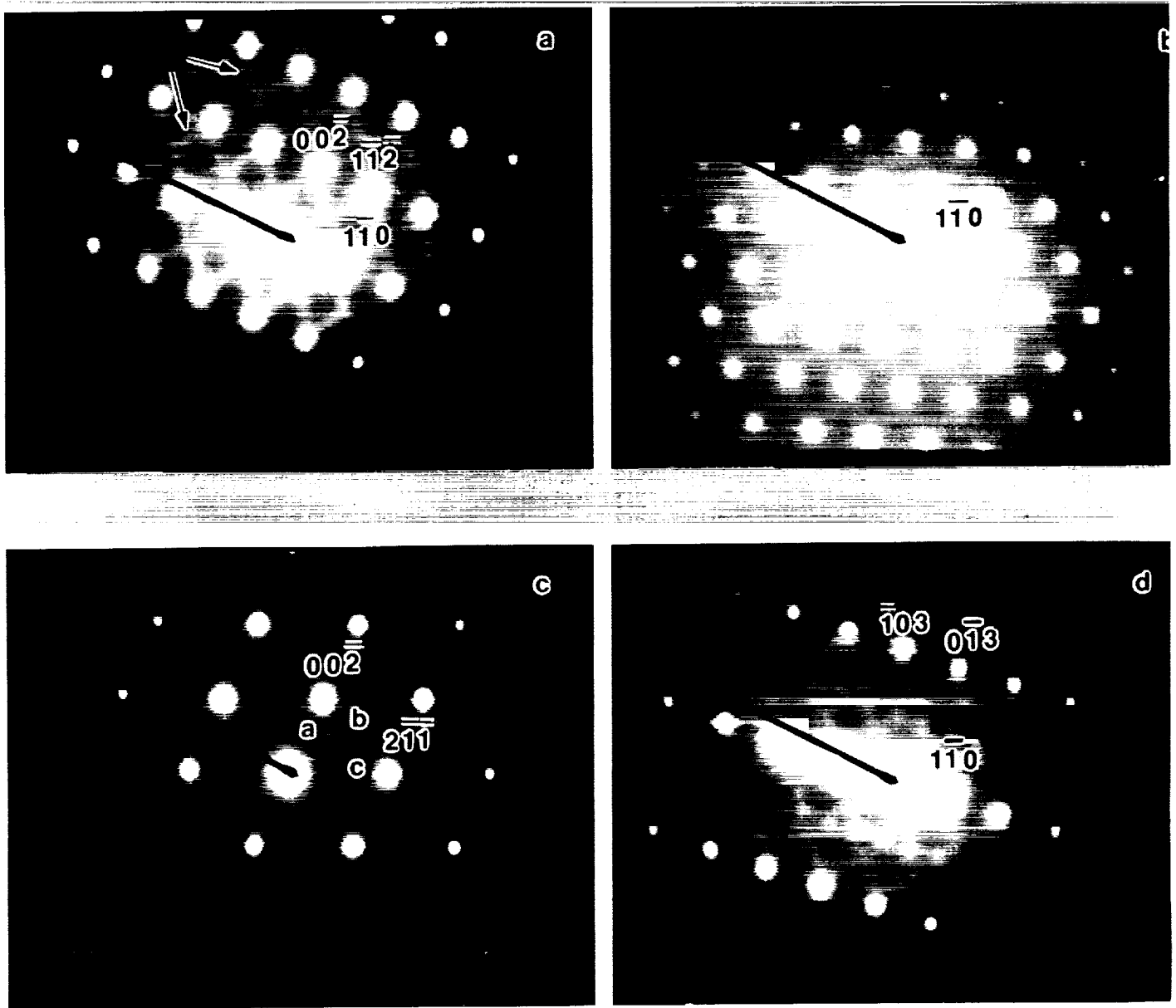


Figure 21. Series of four selected area diffraction patterns (SADP) showing streaking associated with the extremely fine ω -phase (hcp) in the β (bcc) matrix. (a) $\mathbf{B} - (110)_{\beta}$, (b) $\mathbf{B} - (111)_{\beta}$, (c) $\mathbf{B} - (120)_{\beta}$ and (d) $\mathbf{B} - (331)_{\beta}$. The directions of the streaks in each SADP were determined to be in agreement with the ω -phase being distributed in rows along the $\langle 111 \rangle_{\beta} \parallel \langle 0001 \rangle_{\omega}$ direction. The points a, b, and c in (c) correspond $(\bar{1}011)$, $(\bar{2}020)$ and (0001) reflections of the ω -phase.

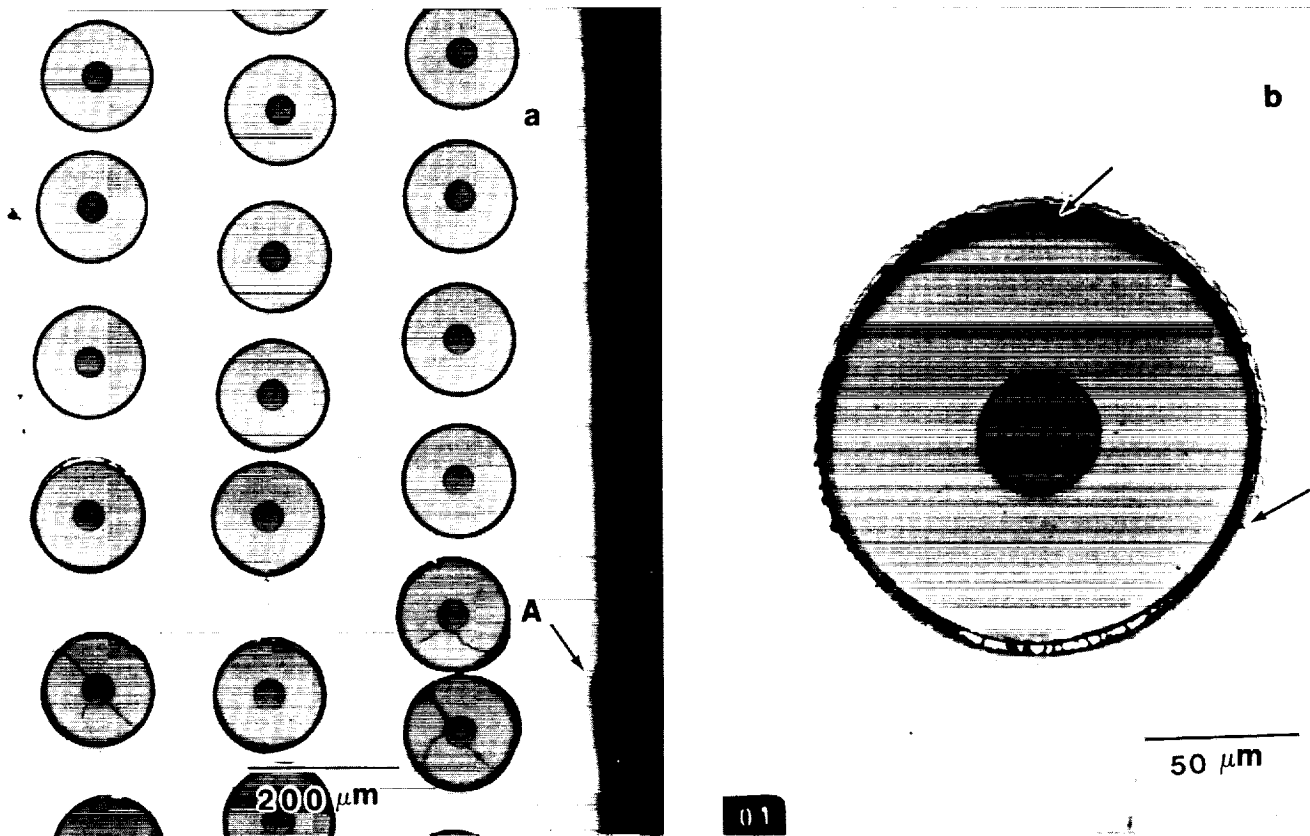


Figure 22. Optical micro-photographs of the edge cross-section of a 90-degree composite, strained to approximately 1.6 percent (Stage III); as-polished sample, and the loading axis is vertical. The higher magnification micrograph (b) illustrates both debonding and cracking of the reaction zone.

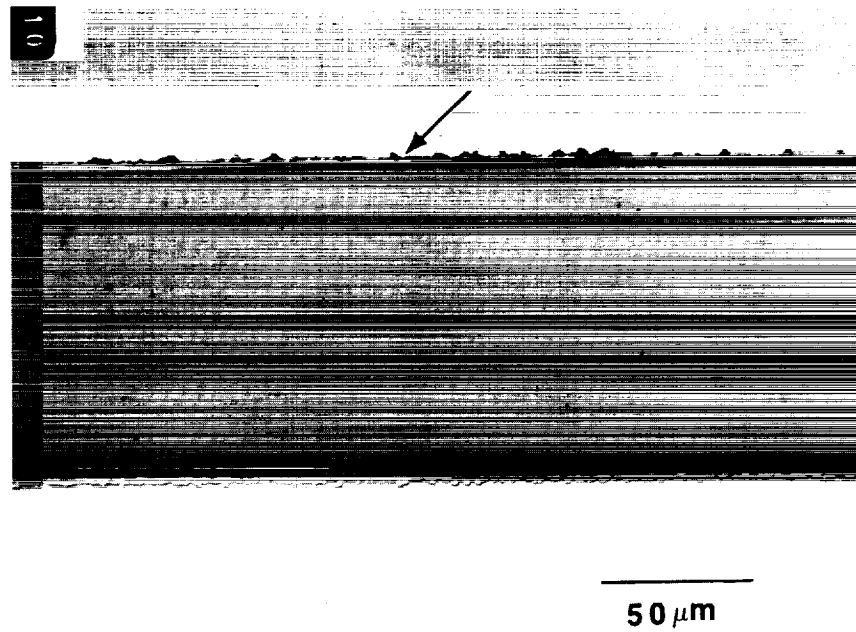


Figure 23. Longitudinal section of a 90-degree composite deformed into Stage III. Debonding and cracking at the fiber-matrix interface is shown by an arrow.

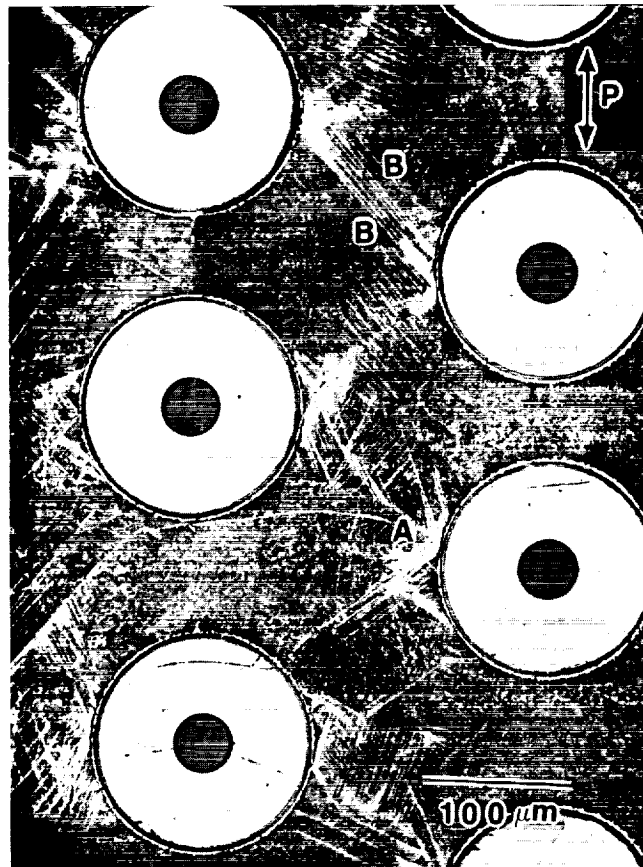


Figure 24. Etched microstructure of a 90-degree specimen, loaded into Stage III. Slip bands are indicated by arrows. Final failure of the composite occurred by crack initiation and failure along the intense shear bands.

ORIGINAL PAGE
BLACK AND WHITE PHOTOGRAPH



Figure 25. Optical photomicrograph of a 90-degree specimen, unloaded from a strain of 0.5 percent (Stage II). The slip bands (white lines) are mostly associated with reaction-zone cracks; the latter, although faint in this figure, are indicated by arrows.

ORIGINAL PAGE
BLACK AND WHITE PHOTOGRAPH

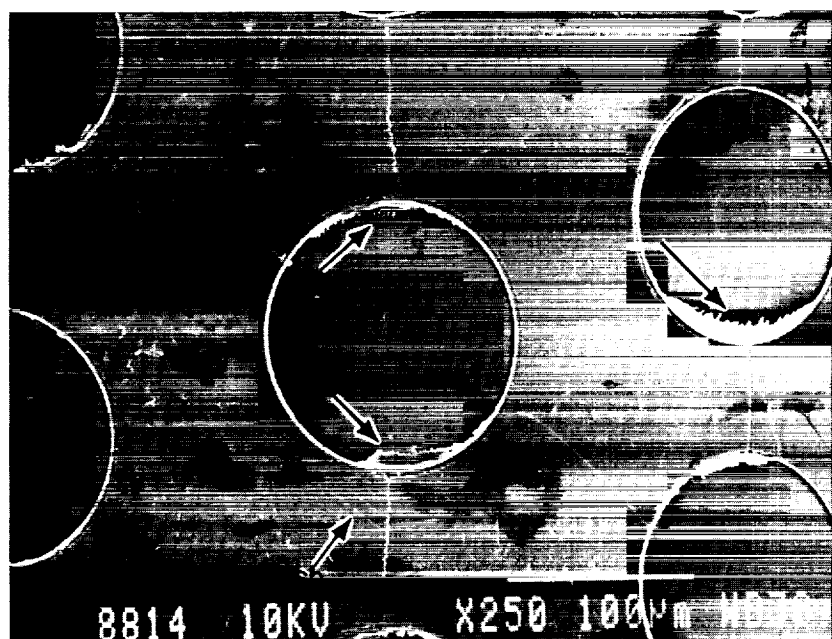


Figure 26. Surface replica of a 90-degree specimen strained to 0.5 percent (Stage II); replica taken at full load. The region indicated by arrow corresponds to the acetate tape entering into the debonded fiber-matrix interface. The loading axis is vertical.

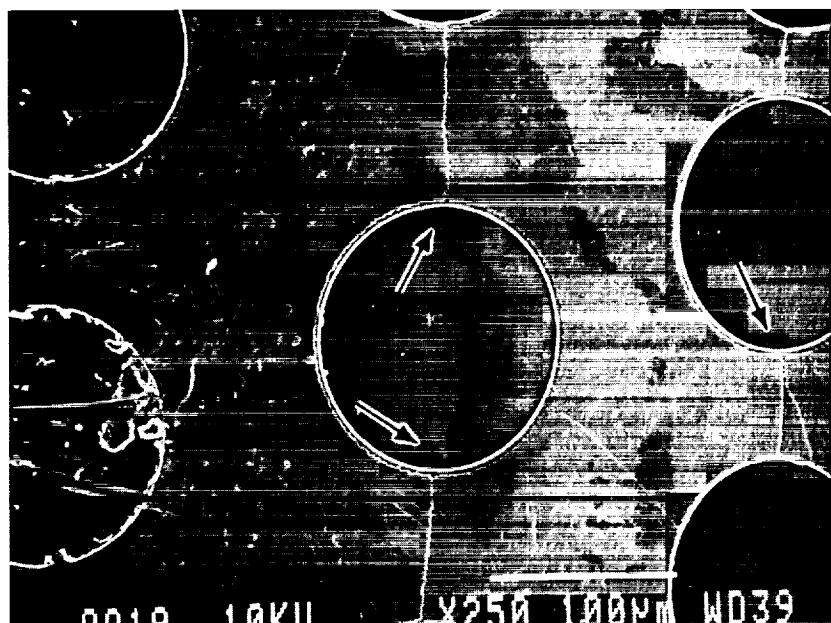


Figure 27. Replica of the same region as Figure 26, after the load had been reduced to zero. There is no acetate tape protruding, indicating that the fiber-matrix separation has largely closed upon unloading.

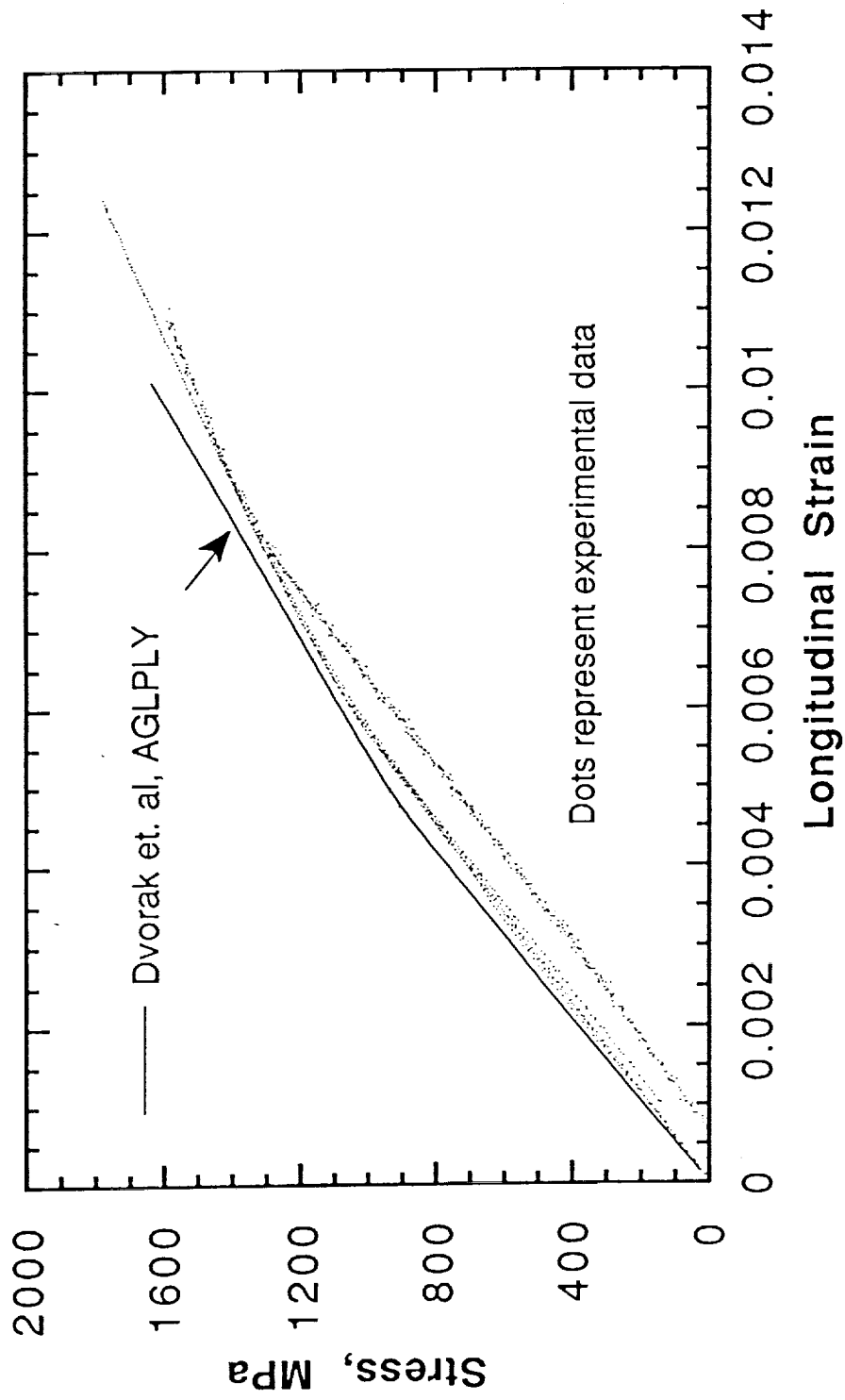
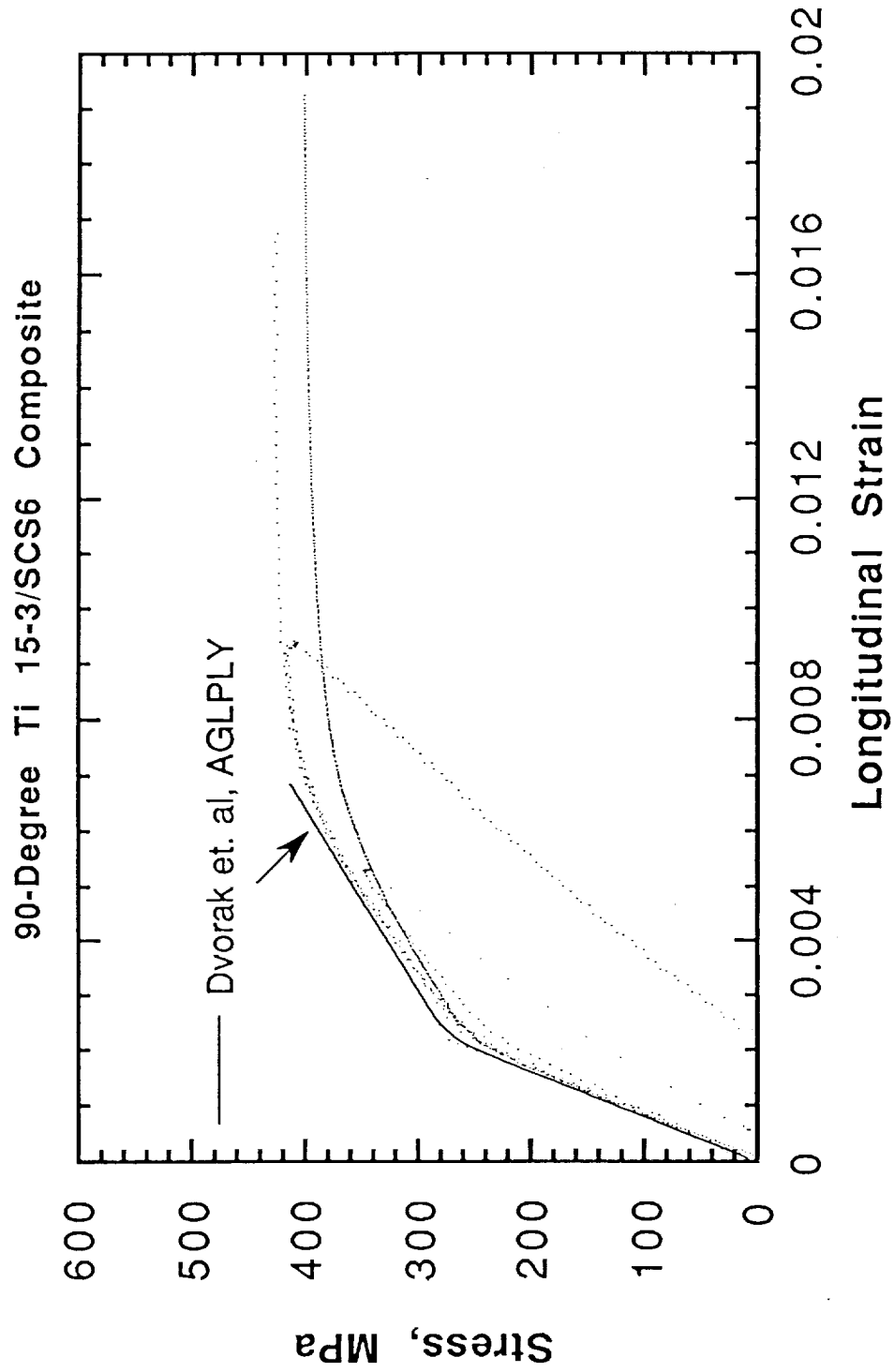
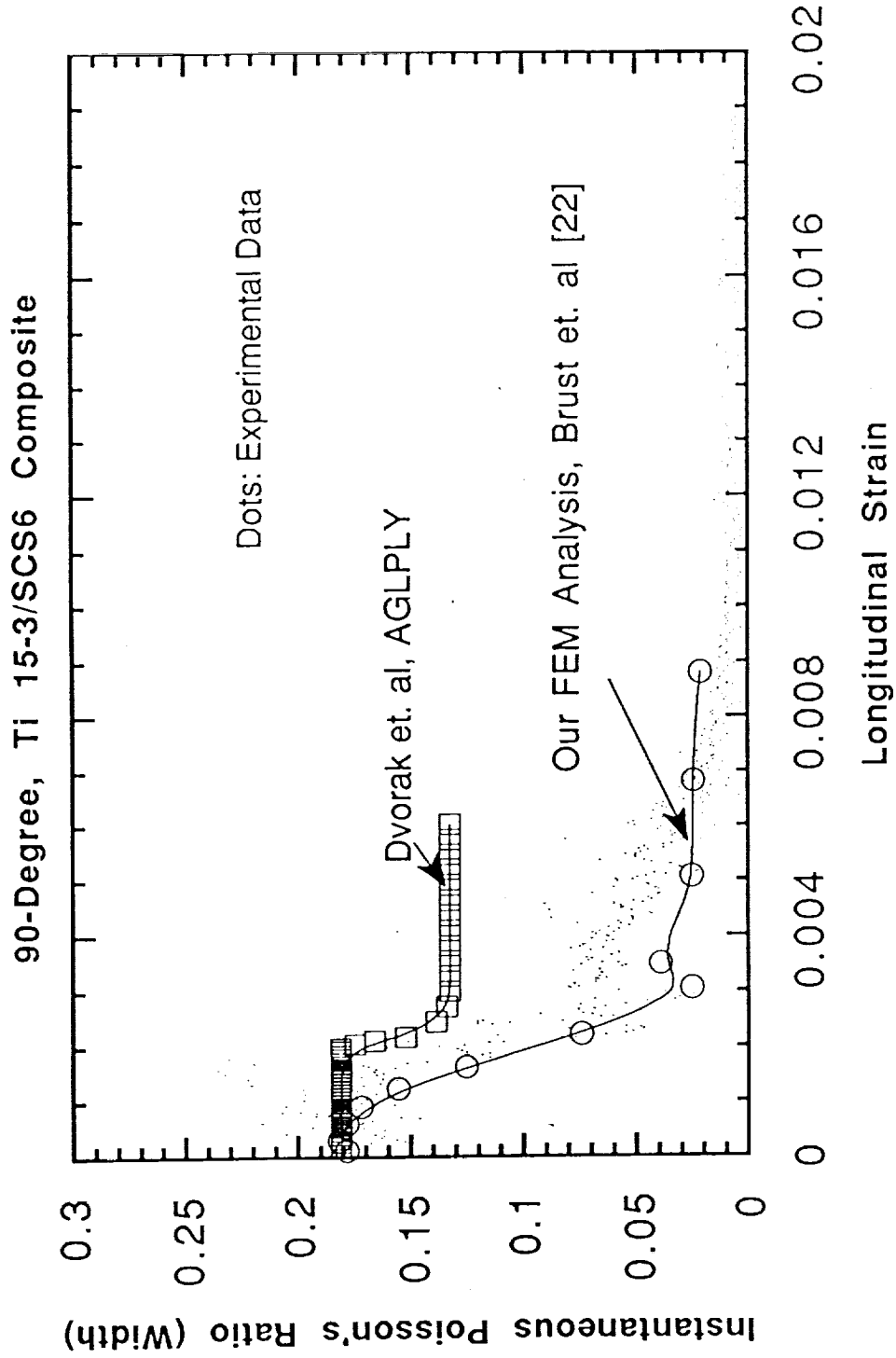


Figure 28. Comparison of model predictions with experimental data for the 0-degree Ti 15-3/SCS6 composite.



90AGLstvs1s.plot

Figure 29. Comparison of model predictions with experimental data for the 90-degree Ti 15-3/SCS6 composite.



FEM90trcpw.plot2

Figure 30. Comparison of model predictions with experimental data for the 90-degree Ti 15-3/SCS6 composite.

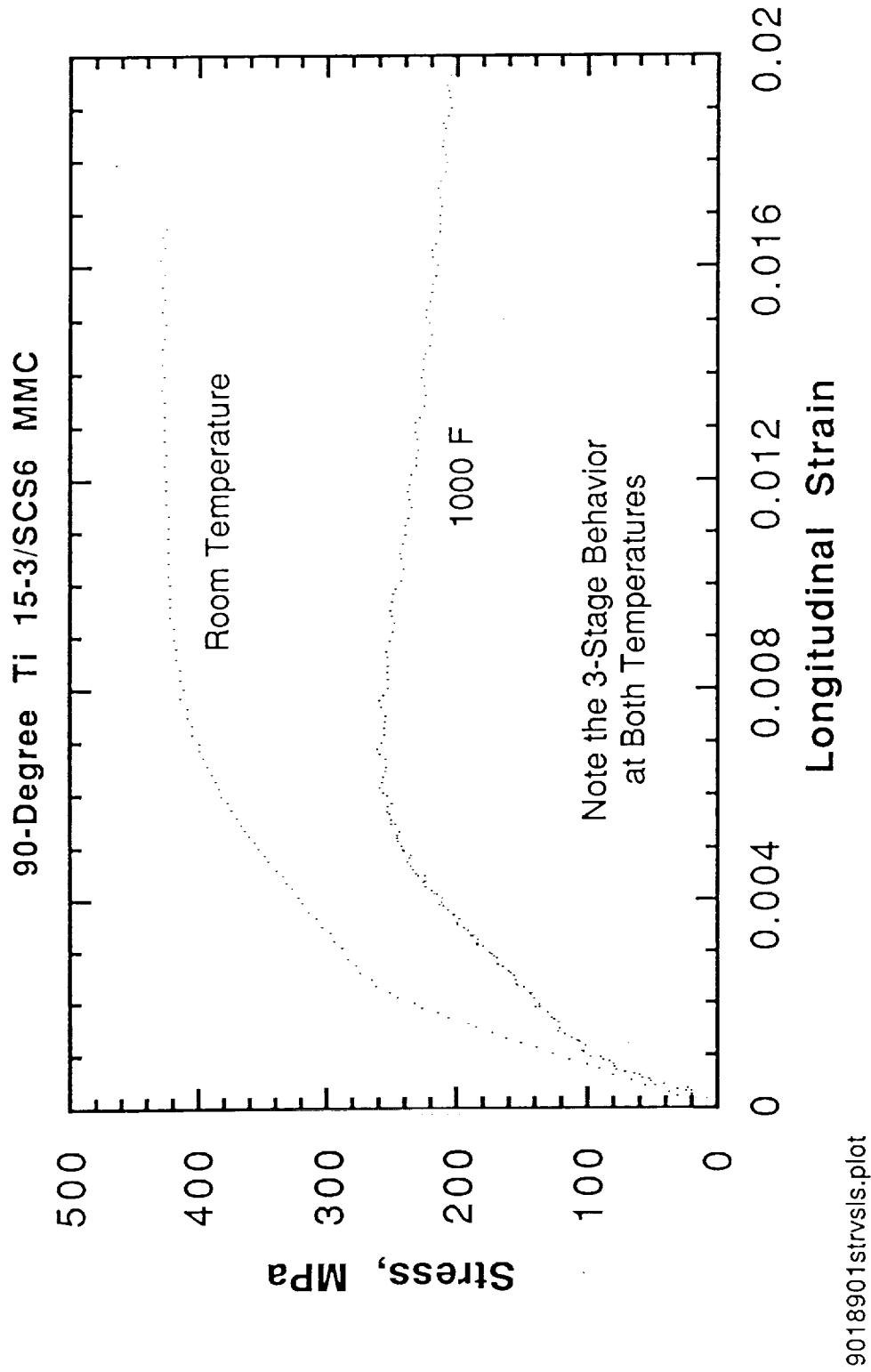


Figure 31. Plot showing effects of temperature on the stress versus longitudinal strain response for the 90-degree composite.

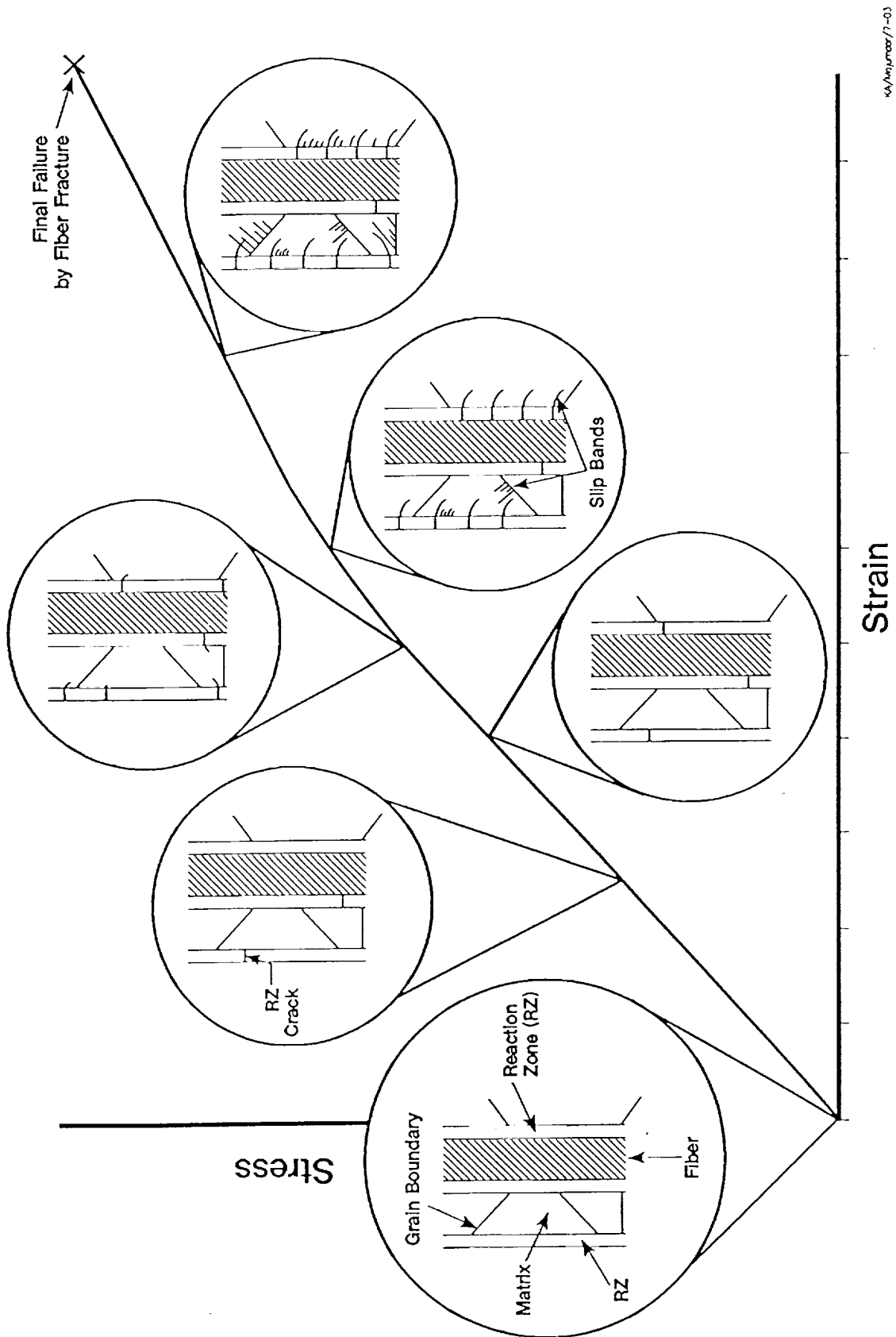
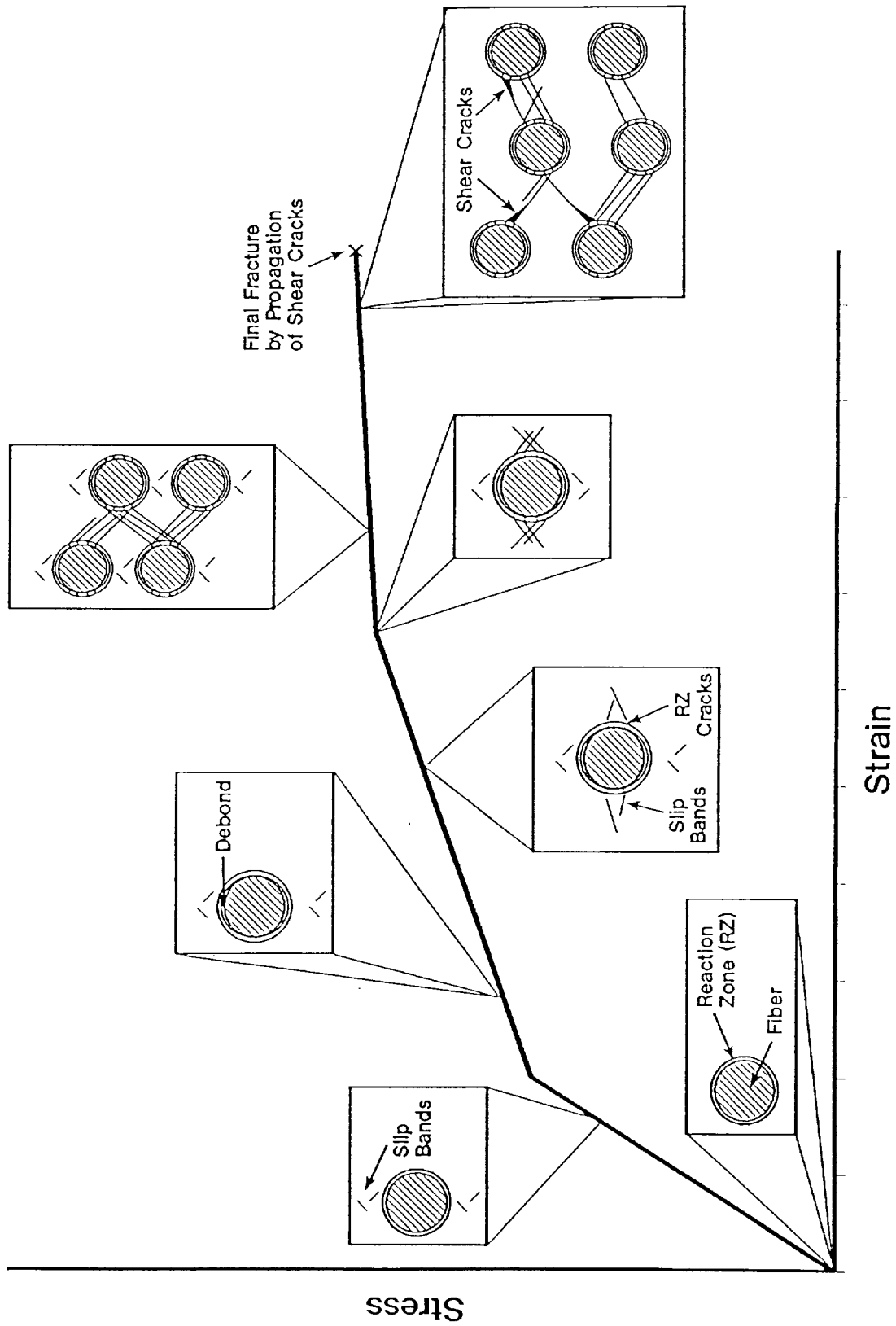


Figure 32. Deformation sequence for the 0-degree composite, based on current observations.



KJ/Nejmdar/7-01

Figure 33. Deformation sequence for the 90-degree composite, based on current observations.

REPORT DOCUMENTATION PAGE			Form Approved OMB No. 0704-0188	
Public reporting burden for this collection of information is estimated to average 1 hour per response, including the time for reviewing instructions, searching existing data sources, gathering and maintaining the data needed, and completing and reviewing the collection of information. Send comments regarding this burden estimate or any other aspect of this collection of information, including suggestions for reducing this burden, to Washington Headquarters Services, Directorate for Information Operations and Reports, 1215 Jefferson Davis Highway, Suite 1204, Arlington, VA 22202-4302, and to the Office of Management and Budget, Paperwork Reduction Project (0704-0188), Washington, DC 20503.				
1. AGENCY USE ONLY (Leave blank)		2. REPORT DATE March 1992		3. REPORT TYPE AND DATES COVERED Final Contractor Report
4. TITLE AND SUBTITLE Inelastic Deformation of Metal Matrix Composites Part I—Plasticity and Damage Mechanisms			5. FUNDING NUMBERS WU-510-01-50 C-NAS3-26053	
6. AUTHOR(S) B.S. Majumdar and G.M. Newaz				
7. PERFORMING ORGANIZATION NAME(S) AND ADDRESS(ES) Battelle Memorial Institute 505 King Avenue Columbus, Ohio 43201-2693			8. PERFORMING ORGANIZATION REPORT NUMBER None	
9. SPONSORING/MONITORING AGENCY NAMES(S) AND ADDRESS(ES) National Aeronautics and Space Administration Lewis Research Center Cleveland, Ohio 44135-3191			10. SPONSORING/MONITORING AGENCY REPORT NUMBER NASA CR-189095	
11. SUPPLEMENTARY NOTES Project Manager, Brad Lerch, Structures Division, NASA Lewis Research Center, (216) 433-5522.				
12a. DISTRIBUTION/AVAILABILITY STATEMENT Unclassified - Unlimited Subject Category 24			12b. DISTRIBUTION CODE	
13. ABSTRACT (Maximum 200 words) The deformation mechanisms of a Ti 15-3/SCS6 (SiC fiber) metal matrix composite (MMC) were investigated using a combination of mechanical measurements and microstructural analysis. The objectives were to evaluate the contributions of plasticity and damage to the overall inelastic response, and to confirm the mechanisms by rigorous microstructural evaluations. The results of room temperature experiments performed on 0-degree and 90-degree systems primarily are reported in this report. Results of experiments performed on other laminate systems and at high temperatures will be provided in a forthcoming report. Inelastic deformation of the 0-degree MMC (fibers parallel to loading direction) was dominated by plasticity of the matrix. Grain boundaries and reaction-zone cracks were found to be important sites for dislocation and slip-band nucleation. In contrast to the 0-degree MMC, inelastic deformation of the 90-degree composite (fibers perpendicular to the loading direction) occurred by both damage and plasticity. This layup system had a characteristic three-stage deformation behavior: Stages I, II, and III. Inelastic deformation in Stage II was dominated by damage, in the form of fiber-matrix debonding and reaction-zone cracks. However, micro-yielding of the matrix also occurred in Stage II. In Stage III, plasticity was largely concentrated in intense shear bands between fibers. These ultimately led to shear crack initiation and failure. The predictions of a continuum elastic-plastic model were compared with the experimental data. The model was adequate for predicting the 0-degree response; however, it was inadequate for predicting the 90-degree response, largely because it neglected damage. The importance of validating constitutive models using a combination of mechanical measurements and microstructural analysis is pointed out. The deformation mechanisms, and the likely sequence of events associated with the inelastic deformation of MMCs, are indicated in this paper.				
14. SUBJECT TERMS Metal matrix composite; Tensile; Deformation; SiC/Ti-15-3			15. NUMBER OF PAGES 66	
			16. PRICE CODE A04	
17. SECURITY CLASSIFICATION OF REPORT Unclassified	18. SECURITY CLASSIFICATION OF THIS PAGE Unclassified	19. SECURITY CLASSIFICATION OF ABSTRACT Unclassified	20. LIMITATION OF ABSTRACT	

